The medium temperature dependence of jet transport coefficient in high-energy nucleus-nucleus collisions*

Man Xie,[1,2,3,†] Qing-Fei Han,[3,‡] Enke Wang,[1,2,3,§] Ben-Wei Zhang,[3,1,¶] and Han-Zhong Zhang[3,1,**]

[1]*Key Laboratory of Atomic and Subatomic Structure and Quantum Control (MOE), Guangdong Basic Research Center of Excellence for Structure and Fundamental Interactions of Matter, Institute of Quantum Matter South China Normal University, Guangzhou 510006, China*

[2]*Guangdong-Hong Kong Joint Laboratory of Quantum Matter, Guangdong Provincial Key Laboratory of Nuclear Science, Southern Nuclear Science Computing Center, South China Normal University, Guangzhou 510006, China*

[3]*Key Laboratory of Quark and Lepton Physics (MOE) and Institute of Particle Physics, Central China Normal University, Wuhan 430079, China*

The medium temperature T dependence of jet transport coefficient $\hat{q}$ is studied via nuclear modification factor $R_{AA}(p_{\rm T})$ and elliptical flow parameter $v_2(p_{\rm T})$ for large transverse momentum $p_{\rm T}$ hadrons in high-energy nucleus-nucleus collisions. Within a next-to-leading order perturbative QCD parton model for hard scatterings with modified fragmentation functions due to jet quenching controlled by $\hat{q}$, we check the suppression as well as the azimuthal anisotropy for large $p_{\rm T}$ hadrons, and extract $\hat{q}$ by global fits to $R_{AA}(p_{\rm T})$ and $v_2(p_{\rm T})$ data in $A+A$ collisions at RHIC and the LHC, respectively. Numerical results from the best fits show that $\hat{q}/T^3$ goes down with the local medium temperature T in the parton jet trajectory. Compared with the case of a constant $\hat{q}/T^3$, the going-down T dependence of $\hat{q}/T^3$ makes a hard parton jet to lose more energy near T_c and therefore strengthens the azimuthal anisotropy for large $p_{\rm T}$ hadrons. As a result, $v_2(p_{\rm T})$ for large $p_{\rm T}$ hadrons is enhanced by about 10% to fit data better at RHIC/LHC. Considering the first-order phase transition from QGP to the hadron phase and additional energy loss in the hadron phase, $v_2(p_{\rm T})$ is again enhanced by 5-10% at RHIC/LHC.

Keywords: Jet quenching, jet transport parameter, hadron suppression, elliptic flow coefficient, energy loss asymmetry.

I. INTRODUCTION

The suppression and azimuthal anisotropy of the high transverse momentum ($p_{\rm T}$) hadrons are two valuable evidences for the existence of the quark-gluon plasma (QGP) that might be created in high-energy nucleus-nucleus collisions performed at both the Relativistic Heavy-Ion Collider (RHIC) [1–3] and the Large Hadron Collider (LHC) [4–12]. When high energy partons propagate through the color-deconfined QGP medium, they will encounter multiple scatterings and lose their energy via the medium-induced gluon radiations. Then the final state hadrons observed in nucleus-nucleus ($A+A$) collisions will be suppressed compared to those observed in proton-proton ($p+p$) collisions. Generally, the suppression strength is given by the nuclear modification factor $R_{AA}(p_{\rm T})$ defined as a ratio of single hadron spectrum in $A+A$ collisions over that in $p+p$ collisions. In a typical non-central $A+A$ collision, the initial geometric anisotropy can be converted into the azimuthal anisotropy in the gluon density distribution of the produced QGP medium, which leads to the azimuthal anisotropy of the total energy loss for energetic jets due to the path length and the gluon density dependence of the jet energy loss. To characterize this anisotropy, one can introduce the elliptic flow coefficient $v_2(p_{\rm T})$ which is defined as the second order Fourier coefficient in the azimuthal angular distribution of final state high $p_{\rm T}$ hadrons. Both of the two observables $R_{AA}(p_{\rm T})$ and $v_2(p_{\rm T})$ for large $p_{\rm T}$ hadrons are the consequence of jet quenching or energy loss [13–20], which are expected to give a consistent jet quenching description.

The strength of jet energy loss is controlled by jet transport coefficient $\hat{q}$, which is proportional to the medium gluon number density ρ and defined as the average transverse momentum broadening $q_{\rm T}$ squared per unit length for jet propagating inside the medium [21],

$$\hat{q} = \rho \int dq_{\rm T}^2 \frac{d\sigma}{dq_{\rm T}^2} q_{\rm T}^2. \tag{1}$$

Quantitative extraction for the energy loss parameter was first performed by JET Collaboration utilizing different theoretical models and different approximations compared to experimental data for single hadron productions at RHIC and the LHC [22]. For simplicity, $\hat{q}/T^3$ is generally assumed as a constant to study bulk matter evolution [23] and the suppression of large $p_{\rm T}$ single hadron and dihadron production [24, 25]. The jet transport coefficient and the mean free path at the initial time are simultaneously extracted for jet energy loss [26]. Comparing the extracted $\hat{q}/T^3$ for the different initial temperatures in the center of QGP between RHIC and the LHC cases, numerical results hint that $\hat{q}/T^3$ decreases slightly with the increasing of the medium temperature [22–26]. MARTINI [27], MCGILL-AMY [28] and other theoretical studies [29, 30] also unfold similar conclusions. In fact, pertur-

* This work is supported in part by the Guangdong Major Project of Basic and Applied Basic Research No. 2020B0301030008 and the Science and Technology Program of Guangzhou No. 2019050001, by the National Science Foundation of China under Grant Nos. 12347130 and 11935007.

† manxie@m.scnu.edu.cn;
‡ hanqingfei@mails.ccnu.edu.cn;
§ wangek@scnu.edu.cn;
¶ bwzhang@mail.ccnu.edu.cn;
** Corresponding author, zhanghz@mail.ccnu.edu.cn.

bative studies with resummed hard-thermal loops in finite-temperature QCD give rise to an additional temperature dependence of $\hat{q}/T^3$ for a fixed value of the strong coupling constant [31, 32]. CUJET model [33, 34] considers there might exist a strong dependence of $\hat{q}/T^3$ on temperature and try to give a systemic description on $R_{AA}(p_{\rm T})$ and $v_2(p_{\rm T})$ simultaneously with a Gaussian-like temperature dependence form of $\hat{q}/T^3$ [35, 36] within the opacity expansion energy loss formalism [37]. There are also many other descriptions and developments for the jet quenching parameter, such as the radiative corrections to $\hat{q}$ [38–40] and nonperturbative calculations for it using the AdS/CFT correspondence at strong coupling in string theory [41–43] and lattice approaches [44–47]. Recently, with newly-developed Bayesian analysis, JETSCAPE has studied the medium temperature, virtuality, and jet energy dependence of $\hat{q}$ via single hadron suppression at RHIC and the LHC energies [48]. Meanwhile, the LIDO model [49] and JETSCAPE [50] also extracted the $\hat{q}$ value with two types of observables, single inclusive hadron and jet suppression. In Ref. [51], with non-parametric prior distribution of $\hat{q}$, using single hadron production, dihadron and γ-hadron correlation data calibrated the temperature-dependent $\hat{q}$. All studies point out that the $\hat{q}/T^3$ should have a larger value at critical temperature T_c.

In this paper, we study on the additional temperature dependence of $\hat{q}/T^3$ via comparing theoretical calculations with experimental data for both $R_{AA}(p_{\rm T})$ and $v_2(p_{\rm T})$ at large $p_{\rm T}$ at RHIC and the LHC. To reveal a clear tendency for the additional temperature dependence, we assume a linear or Gaussian-distribution form for the temperature dependence of $\hat{q}/T^3$ within a high-twist energy loss formalism [52–54]. A (3+1)d ideal hydrodynamic description of the bulk matter evolution is used for the medium expansion, which is outputted in references [55, 56] for $Au+Au$ collisions at 200 GeV and $Pb+Pb$ collisions at 2.76 TeV. The initial condition for the ideal hydrodynamic equations is fixed so that the final bulk hadron spectra from the experiments are reproduced. In order to fit both $R_{AA}(p_{\rm T})$ and $v_2(p_{\rm T})$ simultaneously, we first consider only the QGP phase for jet energy loss and then the hadron phase contribution [23] is also included. Our calculations give a good description to $R_{AA}(p_{\rm T})$ for different temperature dependence schemes of $\hat{q}/T^3$, while theoretical results for $v_2(p_{\rm T})$ underestimate the experimental data. However, comparing to the case with a constant $\hat{q}/T^3$, we find that the going-down temperature dependence of $\hat{q}/T^3$ gives about 10% rise to $v_2(p_{\rm T})$ in the QGP phase, and an additional 10% rise at RHIC and 5% rise at the LHC when hadron phase contribution is included.

The rest of the paper is organized as follows. We first review the next-to-leading-order (NLO) perturbative QCD (pQCD) parton model with the medium modified fragmentation functions in Sec. II. Then shown in Sec. III and Sec. IV are our numerical results fitting to $R_{AA}(p_{\rm T})$ and $v_2(p_{\rm T})$ data for linear and Gaussian temperature dependence of $\hat{q}/T^3$ in QGP phase, respectively. In Sec. V the hadron phase contribution is also included for the linear temperature dependence of $\hat{q}/T^3$. Finally, we conclude in Sec. VI with a summary.

II. NLO PQCD PARTON MODEL WITH MODIFIED FRAGMENTATION FUNCTIONS

Within the NLO pQCD parton model, the collinear factorized differential cross-section of single hadron production in $p+p$ collisions can be factorized into the convolution of parton distribution functions (PDFs), short-distance partonic cross-sections and fragmentation functions (FFs) [57, 58],

$$\frac{d\sigma^h_{pp}}{dyd^2p_{\rm T}} = \sum_{abcd}\int dx_a dx_b f_{a/p}(x_a,\mu^2) f_{b/p}(x_b,\mu^2) \times \frac{1}{\pi}\frac{d\sigma_{ab\to cd}}{d\hat{t}}\frac{D^h_c(z_c,\mu^2)}{z_c} + \mathcal{O}(\alpha_s^3), \quad (2)$$

where $f_{a/p}(x_a,\mu^2)$ is the parton distribution function for the parton a with the momentum fraction x_a from a free nucleon, and we will use CT14 parametrization [59]. The fragmentation function $D^h_c(z_c,\mu^2)$ for a parton in vacuum is given by the AKK parametrization [60], in which z_c is the momentum fraction carried by the outgoing hadrons from the parent parton c. $d\sigma(ab\to cd)/d\hat{t}$ is the parton-parton hard scattering cross section at LO α_s^2. In our numerical simulations, the partonic scattering cross sections will be computed up to NLO implied in $\mathcal{O}(\alpha_s^3)$. The NLO corrections include 1-loop contributions to $2\to 2$ tree level and $2\to 3$ tree level contributions. More detailed discussions on NLO calculations could be found in the reference [61].

In $A+A$ collisions, the cross-section for single hadron production at high transverse momentum is given by [62, 63],

$$\frac{dN^h_{AA}}{dyd^2p_{\rm T}} = \sum_{abcd}\int d^2rt_A(\vec{r})t_B(\vec{r}+\vec{b})\int dx_a dx_b \times f_{a/A}(x_a,\mu^2,\vec{r}) f_{b/B}(x_b,\mu^2,\vec{r}+\vec{b}) \times \frac{1}{\pi}\frac{d\sigma_{ab\to cd}}{d\hat{t}}\frac{\tilde{D}^h_c(z_c,\mu^2,\Delta E_c)}{z_c} + \mathcal{O}(\alpha_s^3), \quad (3)$$

where $t_A(\vec{r}) = \int \rho_A(\vec{r})dz$ is the nuclear thickness function given by the Woods-Saxon distribution and is normalized as $\int d^2rt_A(\vec{r}) = A$. $f_{a/A}(x_a,\mu^2,\vec{r})$ is the nucleus-modified parton distribution function that is assumed to be factorized into the parton distributions in a free nucleon $f_{a/N}(x_a,\mu^2)$ and the nuclear shadowing factor $S_{a/A}(x_a,\mu^2,\vec{r})$ [64, 65],

$$f_{a/A}(x_a,\mu^2,\vec{r}) = S_{a/A}(x_a,\mu^2,\vec{r})\left[\frac{Z}{A}f_{a/p}(x_a,\mu^2) + \left(1-\frac{Z}{A}\right)f_{a/n}(x_a,\mu^2)\right], \quad (4)$$

where Z is the proton number of the nucleus and A is the nucleus mass number. Assuming that the shadowing is proportional to the local nuclear density, the shadowing factor $S_{a/A}(x_a,\mu^2,\vec{r})$ can be obtained using following form [66, 67],

$$S_{a/A}(x_a,\mu^2,\vec{r}) = 1 + [S_{a/A}(x_a,\mu^2)-1]\frac{At_A(\vec{r})}{\int d^2r[t_A(\vec{r})]^2}, \quad (5)$$

where $S_{a/A}(x_a,\mu^2)$ is given from the EPPS16 [68].

The medium-modified fragmentation functions $\tilde{D}_c^h$ can be calcualted as follows [62, 63, 69–71]:

$$\tilde{D}_c^h(z_c,\mu^2,\Delta E_c) = (1-e^{-\langle N_g\rangle})\left[\frac{z_c'}{z_c}D_c^h(z_c',\mu^2) + \langle N_g\rangle\frac{z_g{}'}{z_c}D_g^h(z_g{}',\mu^2)\right] + e^{-\langle N_g\rangle}D_c^h(z_c,\mu^2), \quad (6)$$

where $z_c = p_{\rm T}/p_{\rm Tc}$ is the momentum fraction for a parton fragmenting into a hadron in vacuum. $z_c{}' = p_{\rm T}/(p_{\rm Tc}-\Delta E_c)$ is the rescaled momentum fraction, and denotes that a parton with $p_{\rm Tc}$ propagating through the medium loses energy ΔE_c and fragments into a hadron with $p_{\rm T}$. $z_g{}' = p_{\rm T}/(\Delta E_c/\langle N_g\rangle)$ is the momentum fraction for a radiated gluon fragmenting into a hadron. $\langle N_g\rangle$ is the radiated gluon number.

The parton energy loss caused by medium-induced gluon radiation can be calculated in the higher-twist (HT) approach [52–54]. For a light quark c with initial energy E, the radiative energy loss ΔE_c can be calculated as,

$$\frac{\Delta E_c}{E} = \frac{2C_A\alpha_s}{\pi}\int d\tau\int\frac{dl_{\rm T}^2}{l_{\rm T}^4}\int dz \times\left[1+(1-z)^2\right]\hat{q}\sin^2\left(\frac{l_{\rm T}^2\tau}{4z(1-z)E}\right), \quad (7)$$

where $C_A = 3$, α_s is the strong coupling constant, and $l_{\rm T}$ is the transverse momentum of the radiated gluon. We assume the energy loss of a gluon is simply $9/4$ times that of a quark due to the different color factors for the quark-gluon vertex and gluon-gluon vertex [52]. The average number of radiated gluons from the propagating hard parton is calculated as [72],

$$\langle N_g\rangle = \frac{2C_A\alpha_s}{\pi}\int d\tau\int\frac{dl_{\rm T}^2}{l_{\rm T}^4}\int\frac{dz}{z} \times\left[1+(1-z)^2\right]\hat{q}\sin^2\left(\frac{l_{\rm T}^2\tau}{4z(1-z)E}\right). \quad (8)$$

The HT formalism contains the transverse momentum $l_{\rm T}$ of the radiated gluon, which also indicates changes in the transverse momenta of the partons [15, 73, 74]. In our numerical simulations, we adopt the small angle approximation within the collinear factorization theorem according to Eq. (3). Consequently, we focus solely on the effect of energy loss and assume the parton direction remains unchanged in the fragmentation functions. Such an approximation has been used in many current jet energy loss formalisms and has successfully explained experimental data [49, 50, 75–78].

The parton energy loss and the number of the radiated gluons are both controlled by the jet transport parameter $\hat{q}$ [21]. According to Eq. (1) for $\hat{q}$ proportional to the medium gluon density ρ, one can simply assume a constant value of the scaled jet transport parameter [25, 26],

$$\frac{\hat{q}}{T^3} = \frac{\hat{q}_0}{T_0^3}\frac{p^\mu\cdot u_\mu}{p_0}, \quad (9)$$

where p^μ is the four momentum of the parton, u^μ is the local four flow velocity of the fluid, T is the local temperature of the medium and T_0 is a reference temperature taken as the highest temperature at the center of the medium at the initial time τ_0.

For an additional T dependence of $\hat{q}/T^3$, one can simply assume a linear form like $\hat{q}/T^3 \sim aT+b$. In the following actual calculations, we write the linear form as,

$$\frac{\hat{q}}{T^3} = [(\frac{\hat{q}_0}{T_0^3}-\frac{\hat{q}_c}{{T_c}^3})\frac{T-T_c}{T_0-T_c}+\frac{\hat{q}_c}{{T_c}^3}]\frac{p^\mu\cdot u_\mu}{p_0}. \quad (10)$$

We also check the additional T dependence of $\hat{q}/T^3$ by Gaussian form,

$$\frac{\hat{q}}{T^3} = \frac{\hat{q}_0}{T_0^3}\frac{e^{-(T/T_c-1)^2/(2\sigma_T^2/T_c^2)}}{e^{-(T_0/T_c-1)^2/(2\sigma_T^2/T_c^2)}}\frac{p^\mu\cdot u_\mu}{p_0}. \quad (11)$$

The parameters $\hat{q}_0$, $\hat{q}_c$, and σ_T are introduced to adjust the strength of the additional temperature dependence. $T_c = 170$ MeV is the critical temperature. When $T = T_0$ for Eq. (10), and $\sigma_T^2 = \infty$ for Eq. (11), the two equations both go back to Eq. (9), respectively.

To describe jet quenching in high-energy nucleus-nucleus collisions, one needs to provide the space-time evolution of the jet transport coefficient in Eq. (9, 10, 11) along the parton propagation. In our studies, the dynamical evolution of the medium that governs the space-time evolution of the local temperature T and flow velocity u is obtained using the (3+1)-dimensional hydrodynamic model [55, 56]. This model gives results on the transverse dynamics of the bulk medium in $A+A$ collisions with the initial conditions. Furthermore, the model includes the first order phase transition between the QGP phase and the hadron phase at T_c = 170 MeV and gives the hadron phase fraction $f(\vec{r})$ which is defined as,

$$f(\vec{r}) = \begin{cases} 0 & \text{if T>170 MeV,} \\ 0\sim 1 & \text{if T=170 MeV,} \\ 1 & \text{if T<170 MeV,} \end{cases} \quad (12)$$

where $\vec{r}$ is the jet local position. As the geometry position moves closer to the periphery of the medium or the medium evolution time becomes longer, the hadronic phase fraction gradually increases from 0 to 1 at $T_c = 170$ MeV, determined by the proportion of hadron and parton number density [55, 79, 80]. The energy loss of the jet propagating through both the QGP phase and the hadronic phase can be described by the higher-twist approach simultaneously, except that the $\hat{q}$ in the separate phase is different. To include the contributions to $\hat{q}$ from both QGP and hadron phases, we change Eq. (9), (10) and (11) to be

$$\frac{\hat{q}}{T^3} \to \frac{\hat{q}}{T^3}(1-f)+\frac{\hat{q}_h}{T^3}f, \quad (13)$$

where $\hat{q}_h$ is the jet transport parameter for the hadronic phase. By combining Eq. (12), one can get that for studies exclusively concerning the QGP phase, we consider the pure partonic medium at $T > 170$ MeV, along with the QGP fraction $(1-f)$ in the mixed phase at $T_c = 170$ MeV. For studies on the hadronic phase, we only need to consider the $\frac{\hat{q}_h}{T^3}f$ term that accounts for the contributions from the hadronic phase during the mixed phase, as well as the entire hadronic medium when the temperature is below 170 MeV, until the

system reaches dynamic freeze-out. When the hadron phase is also considered for jet energy loss, the extracted jet transport parameter for the QGP phase is reduced due to a long evolution time of the mixed phase, as shown in Ref. [23].

The jet transport parameter in the hadron phase can be written as [23],

$$\hat{q}_h = \frac{\hat{q}_N}{\rho_N}[\frac{2}{3}\sum_M \rho_M(T) + \sum_B \rho_B(T)], \tag{14}$$

where $\hat{q}_N \approx 0.02$ GeV^2/fm is the extracted jet transport parameter at the center for the cold nucleonic matter of a large nucleus, and $\rho_N \approx 0.17$ fm^{-3} is the nucleon density at the center of the large nucleus [52]. ρ_M and ρ_B are the meson and baryon density in the hadronic resonance gas at a given temperature, respectively. Factor 2/3 represents the ratio of the constituent quark number of the meson and baryon. The hadron density at a given temperature T and zero chemical potential is expressed as [23],

$$\sum_h \rho_h(T) = \frac{T^3}{2\pi^2}\sum_h (\frac{m_h}{T})^2 \sum_{n=1}^{\infty} \frac{\eta_h^{n+1}}{n} K_2(n\frac{m_h}{T}), \tag{15}$$

where $\eta_h = \pm$ for meson (M)/baryon (B). In the following calculations, hadron resonances with mass below 1 GeV are included: 17 kinds of meson, $\pi^+, \pi^-, \pi^0, K^+, K^-, K^0, \overline{K^0}, \eta, \eta^{'}, \rho^+, \rho^-, \rho^0, K^{*+}$, $K^{*-}, K^{*0}, \overline{K^{*0}}, \omega$; and 2 kinds of baryon, p, n. Here, we ignore the contribution of the anti-nucleons to $\hat{q}_h$, which is less than 3%.

III. LINEAR TEMPERATURE DEPENDENCE OF $\hat{q}/T^3$ IN QGP PHASE

With the spectrum in $p+p$ collisions as a baseline, the nuclear suppression factor $R_{AA}(p_{\rm T})$ for single hadron production in $A+A$ collisions can be expressed as [71, 81],

$$R_{AA}(p_{\rm T}) = \frac{dN^h_{AA}/dyd^2p_{\rm T}}{T_{AA}(\vec{b})d\sigma^h_{pp}/dyd^2p_{\rm T}}, \tag{16}$$

where $T_{AA}(\vec{b}) = \int d^2r t_A(\vec{r}) t_B(\vec{r}+\vec{b})$ is the overlap function of two colliding nuclei.

The anisotropy of the final state hadrons in transverse momentum can be quantified by the Fourier expansion of the hadrons distribution in the azimuthal angle. We focus on the second Fourier coefficient, namely elliptic anisotropy coefficient $v_2(p_{\rm T})$, which can be written as [82–87],

$$v_2(p_{\rm T}) = \frac{\int_{-\pi}^{\pi} d\phi cos(2\phi) dN^h_{AA}/dyd^2p_{\rm T}d\phi}{\int_{-\pi}^{\pi} d\phi dN^h_{AA}/dyd^2p_{\rm T}d\phi}, \tag{17}$$

where ϕ is the jet azimuthal angle between the jet's propagating direction and the impact parameter.

In this section, we will use Eq. (10) and (13) with $\hat{q}_h = 0$ to consider the linear temperature dependence of $\hat{q}/T^3$ in QGP phase. χ^2 fitting to both $R_{AA}(p_{\rm T})$ and $v_2(p_{\rm T})$ for hadrons in the middle rapidity region will be performed for different introduced parameters, which is given by,

$$\chi^2 = \sum_{i=1}^{N} \left[(V_{\rm th} - V_{\rm exp})^2/(\sigma^2_{\rm sys} + \sigma^2_{\rm stat})\right], \tag{18}$$

where $V_{\rm th}$ and $V_{\rm exp}$ denote the theoretical and experimental results, and $\sigma_{\rm sys}$ and $\sigma_{\rm stat}$ give systematic and statistical errors for the data, respectively. For a global fit for both $R_{AA}(p_{\rm T})$ and $v_2(p_{\rm T})$, the data number N for the degree of freedom ($d.o.f.$) is the sum of $R_{AA}(p_{\rm T})$ and $v_2(p_{\rm T})$ data numbers. The $\chi^2/d.o.f$ value is minimized to near unity to find the best-fit temperature dependence of $\hat{q}/T^3$ [36]. In the $\chi^2/d.o.f$ calculations, we only select the experimental data points with $p_{\rm T} > 7.5$ GeV$/c$ at both RHIC and the LHC energies to ensure the validity of pQCD parton model.

A. Fit R_{AA} and v_2 at RHIC

Current researches all pointed that the $\hat{q}_c/T_c^3$ at critical temperature has a larger value, and the value of $\hat{q}_0/T_0^3$ at the highest temperature is smaller. Therefore we first choose $\hat{q}_c/T_c^3 \in [3.0, 9.0]$ and $\hat{q}_0/T_0^3 \in [0.2, 5.6]$ with bin size 0.3 and get 399 couples of $(\hat{q}_c/T_c^3, \hat{q}_0/T_0^3)$ for Eq. (10) and (13) with $\hat{q}_h = 0$. To find the limit value of $\hat{q}_0/T_0^3$, we could expand it to 0 phenomenally. So we make 420 times of calculations for the suppression factor $R_{AA}(p_{\rm T})$ as a function of $p_{\rm T}$ for single hadrons produced in the most central 0 - 5% $Au+Au$ collisions at $\sqrt{s_{\rm NN}} = 200$ GeV. Each result for $R_{AA}(p_{\rm T})$ with a given couple of $(\hat{q}_c/T_c^3, \hat{q}_0/T_0^3)$ provides one value of $\chi^2/d.o.f$ to fit to experimental data of $R_{AA}(p_{\rm T})$ [1, 2]. As shown in Fig. 1 (a) is such a 2-dimensional figure for $\chi^2/d.o.f$ as a function of $(\hat{q}_c/T_c^3, \hat{q}_0/T_0^3)$. The different colors represent different fitting values. The $\chi^2/d.o.f$ value is minimized to near unity to find the best-fitting couples of $(\hat{q}_c/T_c^3, \hat{q}_0/T_0^3)$.

The best fittings given by the red region show that the single hadron $R_{AA}(p_{\rm T})$ is more sensitive to the value of $\hat{q}_c/T_c^3$ than $\hat{q}_0/T_0^3$. But the fitting fails to get one unique couple of $(\hat{q}_c/T_c^3, \hat{q}_0/T_0^3)$ for an explicit dependence form of $\hat{q}/T^3$ on T only through the constraint of single hadron $R_{AA}(p_{\rm T})$. To show the different linear temperature dependence of $\hat{q}/T^3$ for the same suppression of single hadrons, we draw in Fig. 1 (b) the gray dashed curves for $\hat{q}/T^3$ as a function of T, which are constrained by the best-fitting region of $\chi^2/d.o.f$.

Among the gray dashed curves, we choose one horizontal line (blue) for a constant $\hat{q}/T^3$ with $(\hat{q}_c/T_c^3, \hat{q}_0/T_0^3) = (5.6, 5.6)$ and one leaning line (red) for a linear T dependence of $\hat{q}/T^3$ with $(\hat{q}_c/T_c^3, \hat{q}_0/T_0^3) = (7.2, 0.0)$. Using these two couples of $(\hat{q}_c/T_c^3, \hat{q}_0/T_0^3)$, we get almost the same $R_{AA}(p_{\rm T})$ in Fig. 1 (c) which shows that the single hadron suppression is a consequence of total jet energy loss and is not sensitive to the T dependence of $\hat{q}/T^3$ in central $Au+Au$ collisions.

Due to the dependence on the jet path length and the medium density in the jet trajectory inside the hot medium, jet energy loss in noncentral $Au+Au$ collisions has azimuthal

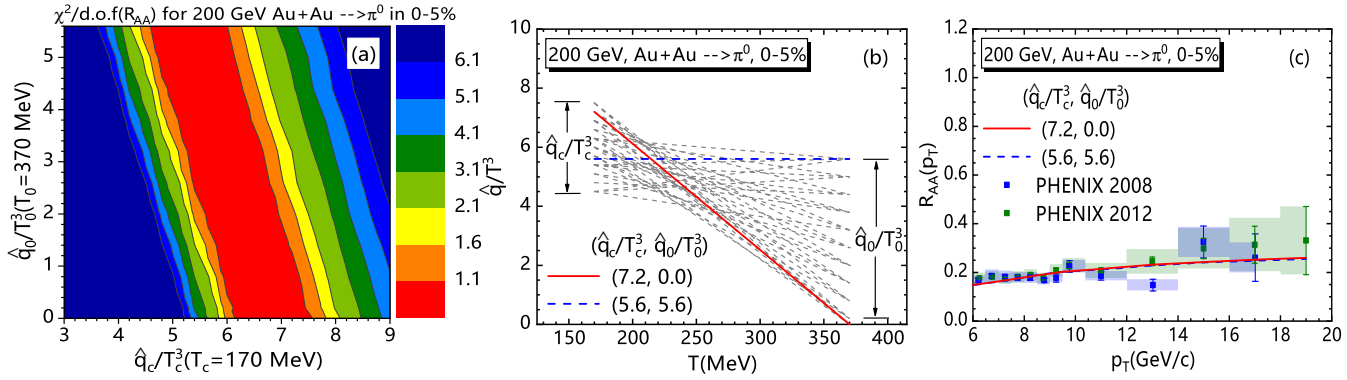

Fig. 1. (Linear-dependence) Panel (a): The $\chi^2/d.o.f$ analyses for single hadron $R_{AA}(p_{\rm T})$ as a function of $\hat{q}_c/T_c^3$ and $\hat{q}_0/T_0^3$ from fitting to PHENIX data [1, 2] in the most central 0 - 5% $Au+Au$ collisions at $\sqrt{s_{\rm NN}}=200$ GeV. Panel (b): The scaled dimensionless jet transport parameters $\hat{q}/T^3$ as a function of medium temperature T from the best fitting region of the panel (a). Panel (c): The single hadron suppression factors $R_{AA}(p_{\rm T})$ with couples of $(\hat{q}_c/T_c^3, \hat{q}_0/T_0^3)=(7.2, 0.0)$ (red solid curve) and $(5.6, 5.6)$ (blue dashed curve) compared with PHENIX [1, 2] data.

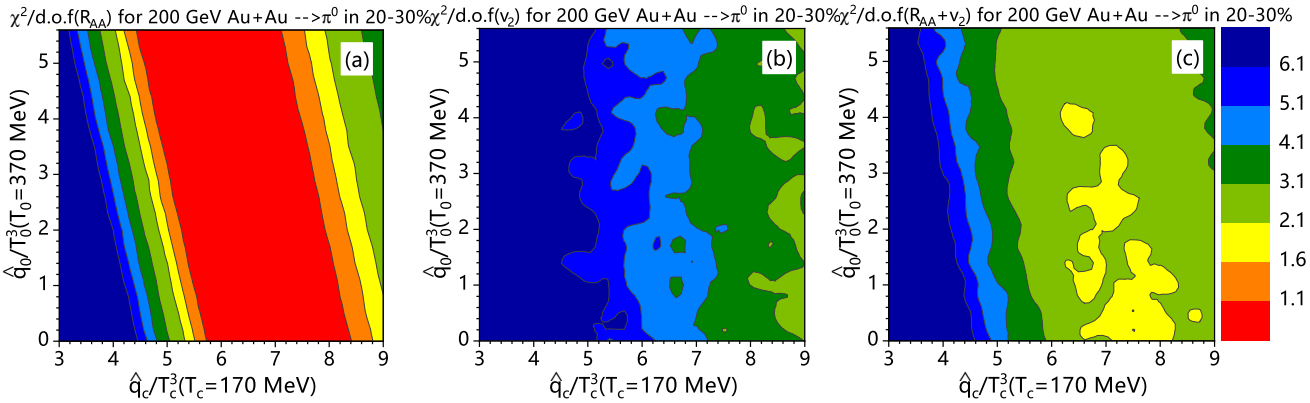

Fig. 2. (Linear-dependence) The $\chi^2/d.o.f$ analyses for single hadron $R_{AA}(p_{\rm T})$ (panel (a)) and elliptic flow $v_2(p_{\rm T})$ (panel (b)) as a function of $\hat{q}_c/T_c^3$ and $\hat{q}_0/T_0^3$ from fitting to experimental data [1–3] in 20 - 30% $Au+Au$ collisions at $\sqrt{s_{\rm NN}}=200$ GeV. The global $\chi^2/d.o.f$ fitting results for both $R_{AA}(p_{\rm T})$ and $v_2(p_{\rm T})$ are shown in the panel (c).

anisotropy. The hadron suppression depends on the azimuthal angle with respect to the reaction plane, thus leading to azimuthal anisotropy in high $p_{\rm T}$ hadron spectra. The same energy loss mechanism permits to make a global fit to constrain $(\hat{q}_c/T_c^3, \hat{q}_0/T_0^3)$ with both the suppression factor $R_{AA}(p_{\rm T})$ and the elliptic flow parameter $v_2(p_{\rm T})$ for large $p_{\rm T}$ hadrons in noncentral $A+A$ collisions. With the same couples of $(\hat{q}_c/T_c^3, \hat{q}_0/T_0^3)$ as in 0 - 5% centrality, we simultaneously make 420 times of calculations for $R_{AA}(p_{\rm T})$ and $v_2(p_{\rm T})$ as a function of $p_{\rm T}$ to fit to the experimental data [1–3] in 20 - 30% $Au+Au$ collisions, and get the $\chi^2/d.o.f$ results for $R_{AA}(p_{\rm T})$ in Fig. 2 (a) and $v_2(p_{\rm T})$ in Fig. 2 (b), respectively. The $\chi^2/d.o.f$ fitting for R_{AA} in noncentral collisions is similar to that in central collisions. This means that only $R_{AA}(p_{\rm T})$ constraint does not give an explicit dependence form of $\hat{q}/T^3$ on T. The $\chi^2/d.o.f$ fitting for v_2 in Fig. 2 (b) shows that the data of elliptic flow $v_2(p_{\rm T})$ favor larger $\hat{q}_c/T_c^3$ and are almost insensitive to $\hat{q}_0/T_0^3$. A global $\chi^2/d.o.f$ fit is performed for both $R_{AA}(p_{\rm T})$ and $v_2(p_{\rm T})$ in Fig. 2 (c) in which the limited yellow region is found to constrain $(\hat{q}_c/T_c^3, \hat{q}_0/T_0^3)$.

Shown in Fig. 3 (a) is the scaled dimensionless jet transport parameters $\hat{q}/T^3$ as a function of medium temperature T from the best fitting region of global χ^2 fits of Fig. 2 (c). The blue dashed curve is also for the constant dependence case with $(\hat{q}_c/T_c^3, \hat{q}_0/T_0^3)=(5.6, 5.6)$, and the red solid curve for a linear T dependence of $\hat{q}/T^3$ with $(\hat{q}_c/T_c^3, \hat{q}_0/T_0^3)=(6.9, 0.0)$. These two dependence forms almost give the same $R_{AA}(p_{\rm T})$ as shown in Fig. 3 (b), which is similar to the situation in central collisions. However, these two different dependence of $\hat{q}/T^3$ gives different contributions to $v_2(p_{\rm T})$ as shown in Fig. 3 (c). Numerical results show that the linearly-decreasing T dependence of $\hat{q}/T^3$ with $(\hat{q}_c/T_c^3, \hat{q}_0/T_0^3)=(6.9, 0.0)$ makes an enhancement by 10% for $v_2(p_{\rm T})$ comparing to the constant dependence case with $(\hat{q}_c/T_c^3, \hat{q}_0/T_0^3)=(5.6, 5.6)$. Such a linearly-decreasing T dependence of $\hat{q}/T^3$ with $(\hat{q}_c/T_c^3, \hat{q}_0/T_0^3)=(6.9, 0.0)$ means more energy loss taking place near the critical temperature T_c.

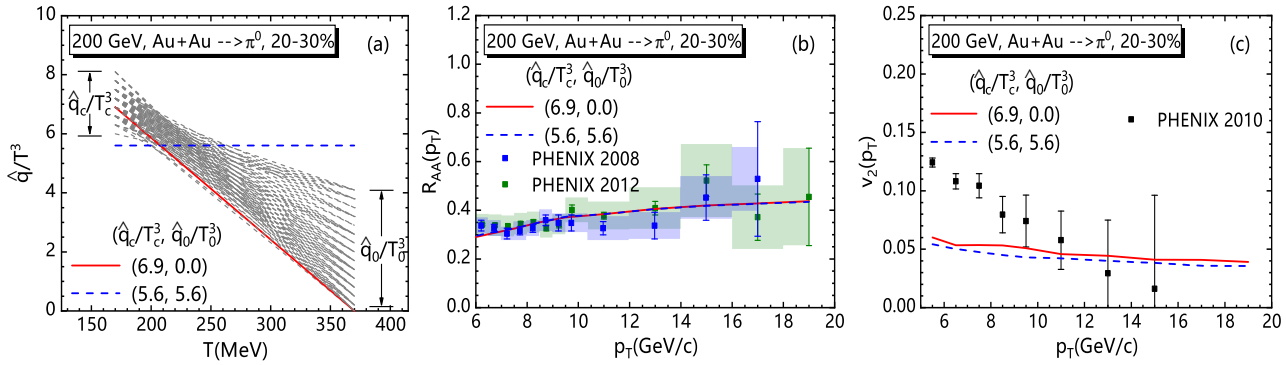

Fig. 3. (Linear-dependence) Panel (a): the scaled dimensionless jet transport parameters $\hat{q}/T^3$ as a function of medium temperature T from the best fitting region of global χ^2 fits of Fig. 2 (c) in 20 - 30% $Au + Au$ collisions at $\sqrt{s_{\rm NN}} = 200$ GeV. The single hadron suppression factors $R_{AA}(p_{\rm T})$ and elliptic flow $v_2(p_{\rm T})$ are shown in panel (b) and (c), respectively, with couples of $(\hat{q}_c/T_c^3, \hat{q}_0/T_0^3) = (6.9, 0.0)$ (red solid curve) and $(5.6, 5.6)$ (blue dashed curve) compared with PHENIX [1–3] data.

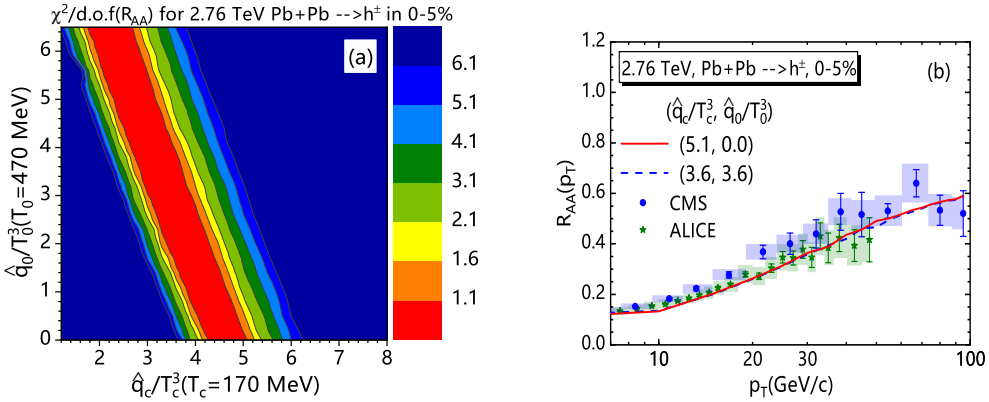

Fig. 4. (Linear-dependence) Panel (a): The $\chi^2/d.o.f$ analyses for single hadron $R_{AA}(p_{\rm T})$ as a function of $\hat{q}_c/T_c^3$ and $\hat{q}_0/T_0^3$ from fitting to experimental data [4, 5] in the most central 0 - 5% $Pb+Pb$ collisions at $\sqrt{s_{\rm NN}} = 2.76$ TeV. Panel (b): The single hadron suppression factors $R_{AA}(p_{\rm T})$ with couples of $(\hat{q}_c/T_c^3, \hat{q}_0/T_0^3) = (5.1, 0.0)$ (red solid curve) and $(3.6, 3.6)$ (blue dashed curve) compared with experimental data.

B. Fit R_{AA} and v_2 at the LHC

Similarly, we present our relevant results for $Pb + Pb$ collisions at $\sqrt{s_{\rm NN}} = 2.76$ TeV. Here we choose $\hat{q}_c/T_c^3 \in [1.2, 8.1]$ and $\hat{q}_0/T_0^3 \in [0.2, 6.5]$ with the same bin size 0.3 and further include the $\hat{q}_0/T_0^3 = 0.0$, thus get 552 couples of $(\hat{q}_c/T_c^3, \hat{q}_0/T_0^3)$ for Eq. (10) and (13) with $\hat{q}_h = 0$. The $\chi^2/d.o.f$ results for central 0 - 5% $Pb + Pb$ collisions are performed on single hadron suppression factors, as shown in Fig. 4 (a). The best-fitting contour is similar to that in Fig. 1 (a) but with a smaller $\hat{q}_c/T_c^3$. With a constant form and a linear form for $\hat{q}/T^3$, we again obtain the same single hadron suppression as shown in Fig. 4 (b).

For 20 - 30% $Pb + Pb$ collisions, the $\chi^2/d.o.f$ fitting for only $R_{AA}(p_{\rm T})$ or $v_2(p_{\rm T})$, and the global fitting for both of them are shown in Fig. 5 (a), (b) and (c), respectively. Similar to noncentral $Au + Au$ collisions, both the separated $\chi^2/d.o.f$ fitting for $R_{AA}(p_{\rm T})$ and $v_2(p_{\rm T})$ can not give clear constrain on the T dependence of $\hat{q}/T^3$. However, the difference from $\chi^2/d.o.f(R_{AA})$, $\chi^2/d.o.f(v_2)$ shows that data of $v_2(p_{\rm T})$ prefer larger jet energy loss near T_c and are insensitive to the change of $\hat{q}_0/T_0^3$. Consequently, the global fits for both $R_{AA}(p_{\rm T})$ and $v_2(p_{\rm T})$ make the constrain to some extent on the T dependence of $\hat{q}/T^3$ as shown in Fig. 5 (c), similarly to Fig. 2 (c).

Choosing $\chi^2/d.o.f < 1.6$ in Fig. 5 (c) for the best fitting, one can get the curves for the T dependence of $\hat{q}/T^3$ in Fig. 6 (a). We again get a tendency for $\hat{q}/T^3$ to decrease with the increasing local temperature in the jet trajectory. Among the best-fitting values, selecting $(\hat{q}_c/T_c^3, \hat{q}_0/T_0^3) = (5.4, 0.0)$ for the linear T dependence and $(4.1, 4.1)$ for the constant dependence, we calculate the $R_{AA}(p_{\rm T})$ and $v_2(p_{\rm T})$ as a function of $p_{\rm T}$ shown in Fig. 6 (b) and (c), respectively. Two almost same $R_{AA}(p_{\rm T})$ are obtained, while the $v_2(p_{\rm T})$ has an enhancement by 10% due to the larger jet energy loss near T_c for the linearly-decreasing T dependence of $\hat{q}/T^3$ at the LHC.

No matter whether in $Pb+Pb$ collisions or $Au+Au$ colli-

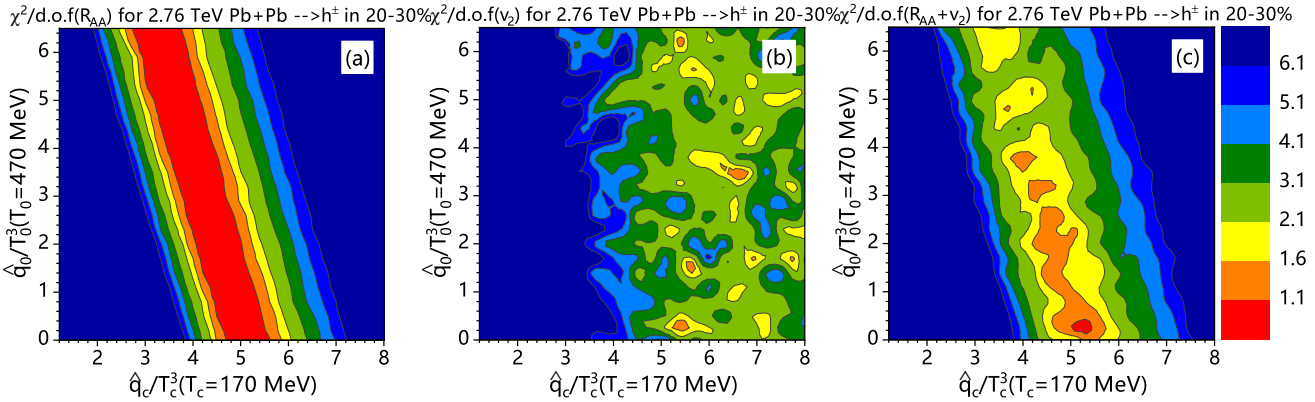

Fig. 5. (Linear-dependence) The $\chi^2/d.o.f$ analyses of single hadron $R_{AA}(p_{\rm T})$ (panel (a)) and elliptic flow $v_2(p_{\rm T})$ (panel (b)) as a function of $\hat{q}_c/T_c^3$ and $\hat{q}_0/T_0^3$ from fitting to experimental data [4, 5, 9, 10] in 20 - 30% $Pb+Pb$ collisions at $\sqrt{s_{\rm NN}} = 2.76$ TeV. The global $\chi^2/d.o.f$ fitting results for both $R_{AA}(p_{\rm T})$ and $v_2(p_{\rm T})$ are shown in the panel (c).

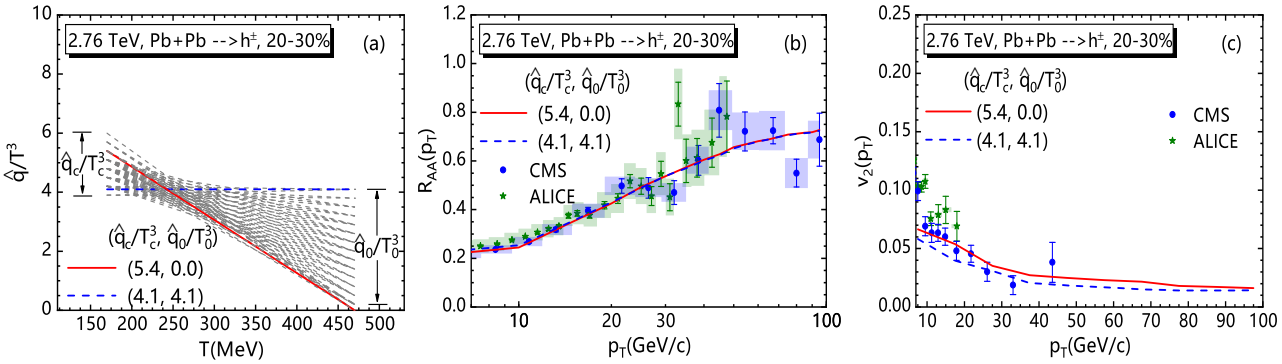

Fig. 6. (Linear-dependence) In 20 - 30% $Pb+Pb$ collisions at $\sqrt{s_{\rm NN}} = 2.76$ TeV, the scaled dimensionless jet transport parameters $\hat{q}/T^3$ as a function of medium temperature T from the best fitting region of global χ^2 fits of Fig. 5 (c) are shown in the panel (a). The single hadron suppression factors $R_{AA}(p_{\rm T})$ and elliptic flow $v_2(p_{\rm T})$ are shown in the (b) and (c) panels, respectively, with couples of $(\hat{q}_c/T_c^3, \hat{q}_0/T_0^3) = (5.4, 0.0)$ (red soild curve) and $(4.1, 4.1)$ (blue dashed curve) compared with experimental data [4, 5, 9, 10].

sions, $R_{AA}(p_{\rm T})$ and $v_2(p_{\rm T})$ are both more sensitive to the jet energy loss near critical temperature T_c than near the initial highest temperature T_0. Relatively, the data of $v_2(p_{\rm T})$ prefer a larger value of $\hat{q}_c/T_c^3$. Furthermore, the anisotropy of final state hadrons at high transverse momentum can be strengthened up to 10% by increasing the jet energy loss near T_c with the linearly-decreasing T dependence of $\hat{q}/T^3$.

C. Jet energy loss distribution

Given a parton jet with any creation site and any moving direction in the initial hard scattering, let us see the jet energy loss distribution when propagating through the hot medium. The average energy loss rate in the jet trajectory is given by,

$$\langle\frac{d\Delta E}{d\tau}\rangle = \frac{\int d\phi \int d^2r t_A(\vec{r}) t_B(\vec{r}+\vec{b}) d\Delta E(\vec{r}+\vec{n}\tau)/d\tau}{\int d\phi \int d^2r t_A(\vec{r}) t_B(\vec{r}+\vec{b})}, \tag{19}$$

where $\Delta E(\vec{r})$ is given by Eq. (7), $\vec{r}$ is the initial creation point for an energy-given jet, and $\vec{n}$ is the unit vector of the jet moving direction ϕ which is the same as that in Eq. (17). The average accumulative energy loss for the jet traversing through the medium is then given as,

$$\langle\Delta E(\tau)\rangle = \frac{\int d\phi \int d^2r t_A(\vec{r}) t_B(\vec{r}+\vec{b}) \int_{\tau_0}^{\tau} d\tau \frac{d\Delta E(\vec{r}+\vec{n}\tau)}{d\tau}}{\int d\phi \int d^2r t_A(\vec{r}) t_B(\vec{r}+\vec{b})}. \tag{20}$$

Shown in Fig. 7 are the average accumulative (solid curves) and differential (dashed curves) energy loss for one 10 GeV jet with $(\hat{q}_c/T_c^3, \hat{q}_0/T_0^3) = (6.9, 0.0)$ (red curves) and $(5.6, 5.6)$ (blue curves) in 20 - 30% $Au+Au$ collisions at $\sqrt{s_{\rm NN}} = 200$ GeV (panel (a) and (b)), and for one 100 GeV jet with $(\hat{q}_c/T_c^3, \hat{q}_0/T_0^3) = (5.4, 0.0)$ (red curves) and $(4.1, 4.1)$ (blue curves) in 20 - 30% $Pb+Pb$ collisions at $\sqrt{s_{\rm NN}} = 2.76$ TeV (panel (d) and (e)), respectively. The medium temperature as a function of time at the center point $(x, y) = (0, 0)$ for the two collision systems are shown in the

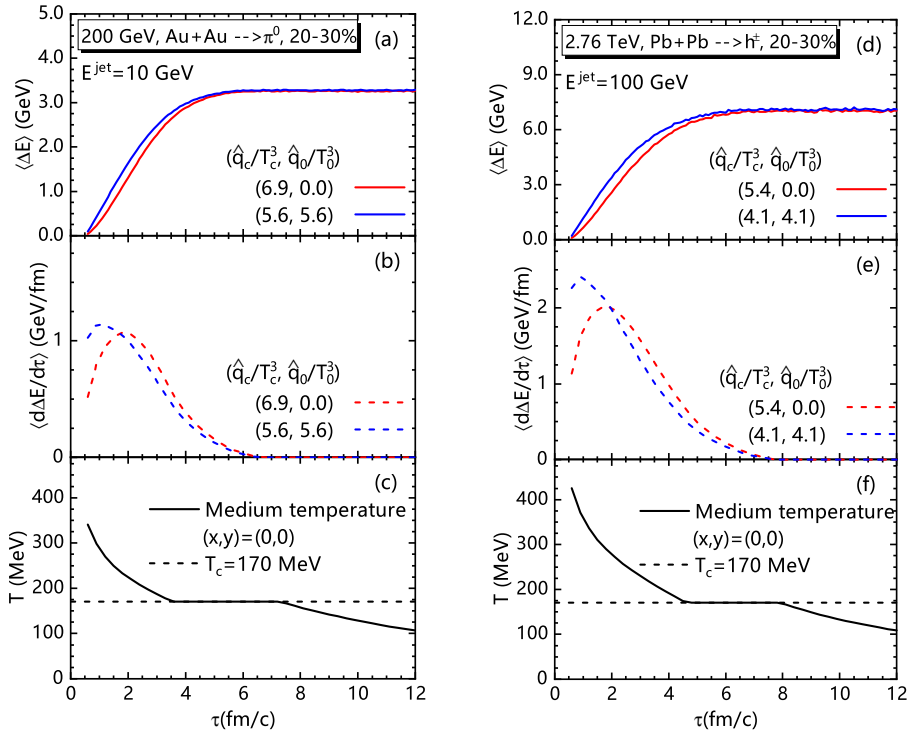

Fig. 7. (Linear-dependence) Panels (a) and (d): the average accumulative energy loss for one 10 GeV jet in 20 - 30% $Au + Au$ collisions at $\sqrt{s_{\rm NN}} = 200$ GeV and for one 100 GeV jet in 20 - 30% $Pb + Pb$ collisions at $\sqrt{s_{\rm NN}} = 2.76$ TeV, respectively. Panels (b) and (e): the corresponding differential energy loss. Red solid or dashed curves are for the linearly-decreasing T dependence of $(\hat{q}/T^3$, and blue for the constant $(\hat{q}/T^3$. Panels (c) and (f): the medium temperature as a function of time at the center point $(x, y) = (0, 0)$ for the two collision systems, respectively.

lower panels (c) and (f), respectively.

When the jet passes out of the critical region from QGP to the hadron phase, it is over for the jet to accumulate the lost energy, as shown in Eq. (13) with $\hat{q}_h = 0$. For the well-chosen two cases of the constant dependence and the linearly-decreasing T dependence of $\hat{q}/T^3$, the final total energy loss is exactly similar, as shown in Fig. 7 (a) and (d). In the meantime, the peak of the jet energy loss distribution $\langle d\Delta E/d\tau\rangle$ along the jet path is "pushed" to move to critical temperature T_c nearby due to the linearly-decreasing T dependence of $\hat{q}/T^3$ (red dashed curves) compared to the constant dependence (blue dashed curves), as shown in Fig. 7 (b) and (e). More energy loss happens on the approaching critical temperature and enhances the final hadron azimuthal anisotropy, so $v_2(p_{\rm T})$ is strengthened up for the linearly-decreasing T dependence case, as shown in Fig. 3 (c) and Fig. 6 (c).

In order to clearly illustrate the enhanced azimuthal anisotropy, we define the energy loss asymmetry below,

$$A\langle\Delta E(\tau)\rangle = \frac{\langle\Delta E(\tau)\rangle^{\phi=\pi/2} - \langle\Delta E(\tau)\rangle^{\phi=0}}{\langle\Delta E(\tau)\rangle^{\phi=\pi/2} + \langle\Delta E(\tau)\rangle^{\phi=0}}, \quad (21)$$

where $\langle\Delta E(\tau,\phi)\rangle$ is given by Eq. (20) in which the ϕ integration for the azimuthal average is removed. On average, a parton jet will encounter the most energy loss due to the longest path length at $\phi = \pi/2$ and the least at $\phi = 0$. Shown in Fig. 8 (a) and (b) are such energy loss asymmetries for an energy-given parton jet in 20 - 30% $Au + Au$ at 200 GeV and $Pb + Pb$ collisions at 2.76 TeV, respectively. The red solid curves are for the case of the linearly-decreasing T dependence of $\hat{q}/T^3$, while the blue solid curves are for the constant case. The former is 10% larger than the latter in both panels, which is similar to the enhancement for $v_2(p_{\rm T})$ in Fig. 3 (c) and 6 (c).

Due to the medium temperature evolution, different T dependence of jet transport coefficient gives different energy loss distribution for jet propagation. The large $p_{\rm T}$ hadron suppression R_{AA} is a consequence of total energy loss and independent of the jet energy loss distribution. However, compared to the constant case for a given total energy loss, the linearly-decreasing T dependence of $\hat{q}/T^3$ makes an energy loss to redistribute and leads to more energy loss happening near the critical temperature and, therefore, more stronger azimuthal anisotropy for hadron production.

IV. GAUSSIAN TEMPERATURE DEPENDENCE OF $\hat{q}/T^3$ IN QGP PHASE

In the last section, numerical results for the linear T dependence assumption show that $\hat{q}/T^3$ goes down with the

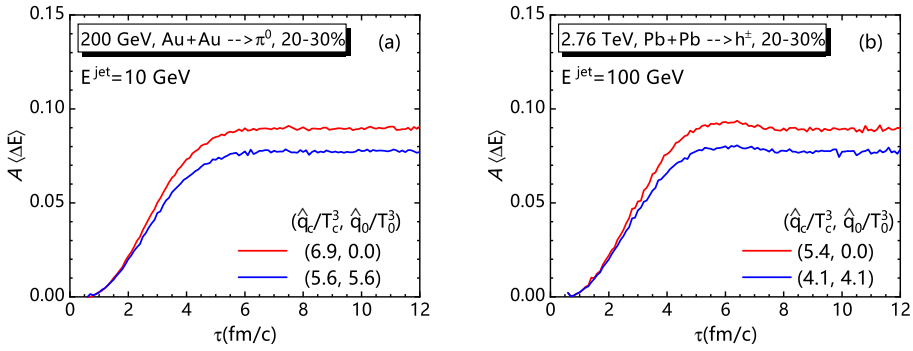

Fig. 8. (Linear-dependence) The energy loss asymmetry between the jet propagating direction of $\phi = \pi/2$ and $\phi = 0$ for one 10 GeV jet with $(\hat{q}_c/T_c^3, \hat{q}_0/T_0^3) = (6.9, 0.0)$ (red curve) and $(5.6, 5.6)$ (blue curve) in 20 - 30% $Au+Au$ collisions at $\sqrt{s_{\rm NN}} = 200$ GeV (panel (a)) and for one 100 GeV jet with $(\hat{q}_c/T_c^3, \hat{q}_0/T_0^3) = (5.4, 0.0)$ (red curve) and $(4.1, 4.1)$ (blue curve) in 20 - 30% $Pb+Pb$ collisions at $\sqrt{s_{\rm NN}} = 2.76$ TeV (panel (b)).

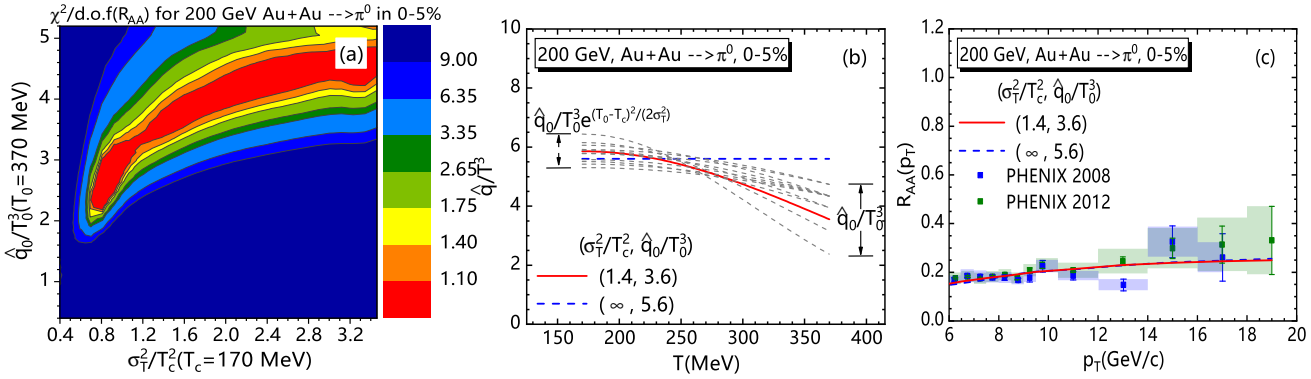

Fig. 9. (Gaussian-dependence) Panel (a): The $\chi^2/d.o.f$ analyses for single hadron $R_{AA}(p_{\rm T})$ as a function of σ_T^2/T_c^2 and $\hat{q}_0/T_0^3$ from fitting to experimental data [1, 2] in the most central 0 - 5% $Au + Au$ collisions at $\sqrt{s_{\rm NN}} = 200$ GeV. Panel (b): The scaled dimensionless jet transport parameters $\hat{q}/T^3$ as a function of medium temperature T from the best fitting region of the panel (a). Panel (c): The single hadron suppression factors $R_{AA}(p_{\rm T})$ with couples of $(\sigma_T^2/T_c^2, \hat{q}_0/T_0^3) = (1.4, 3.6)$ (red solid curve) and $(\sigma_T^2/T_c^2, \hat{q}_0/T_0^3) = (\infty, 5.6)$ (blue dashed curve) compared with PHENIX [1, 2] data.

medium temperature increase. The going-down T dependence of $\hat{q}/T^3$ stimulates an attempt for a Gaussian assumption for the T dependence of $\hat{q}/T^3$. Here we assume the apex of the Gaussian distribution is seated at the critical temperature, as shown in Eq. (11). This assumption for the Gaussian temperature dependence will be submitted into Eq. (13) with $\hat{q}_h = 0$ for the QGP phase only, and the Eq. (7) and (8) for jet energy loss.

A. Fit R_{AA} and v_2 at RHIC

In Eq. (11) for the assumption of the Gaussian temperature dependence, the introduced $\hat{q}_0/T_0^3$ is still the scaled jet transport parameter in the initial time at the center of the medium, while σ_T^2/T_c^2 is the squared Gaussian width. Starting with $Au + Au$ collisions at $\sqrt{s_{\rm NN}} = 200$ GeV, we choose $\sigma_T^2/T_c^2 \in [0.35, 3.5]$ with bin size 0.35 and $\hat{q}_0/T_0^3 \in [0.4, 5.2]$ with bin size 0.4 and get 130 couples of $(\sigma_T^2/T_c^2, \hat{q}_0/T_0^3)$ for Eq. (11) and (13) with $\hat{q}_h = 0$. We firstly get the $R_{AA}(p_{\rm T})$ in 0 - 5% collisions and compare with data [1, 2] to get a 2-dimensional contour plot for the $\chi^2/d.o.f$ fitting, as shown in Fig. 9 (a). According to the obtained best fitting region for $(\sigma_T^2/T_c^2, \hat{q}_0/T_0^3)$, we give $\hat{q}/T^3$ as a function of T in Fig. 9 (b). The red solid curve is for a going-down $\hat{q}/T^3$ dependence with $(\sigma_T^2/T_c^2, \hat{q}_0/T_0^3) = (1.4, 3.6)$ while the blue dashed curve is for a constant dependence with $(\sigma_T^2/T_c^2, \hat{q}_0/T_0^3) = (\infty, 5.6)$. Such two dependence forms give almost the same $R_{AA}(p_{\rm T})$, as shown in Fig. 9 (c). $R_{AA}(p_{\rm T})$ doesn't "care" whether $\hat{q}/T^3$ is of Gaussian temperature dependence or not at RHIC.

Shown in Fig. 10 (a) and (b) are the $\chi^2/d.o.f$ analyses of single hadron $R_{AA}(p_{\rm T})$ and elliptic flow $v_2(p_{\rm T})$ as a function of σ_T^2/T_c^2 and $\hat{q}_0/T_0^3$ from fitting to experimental data [1–3] in 20 - 30% $Au + Au$ collisions at $\sqrt{s_{\rm NN}} = 200$ GeV, respectively. The global $\chi^2/d.o.f$ fitting results for both $R_{AA}(p_{\rm T})$ and $v_2(p_{\rm T})$ are shown in Fig. 10 (c). Although $\chi^2/d.o.f(R_{AA})$ performs inactively for the tempera-

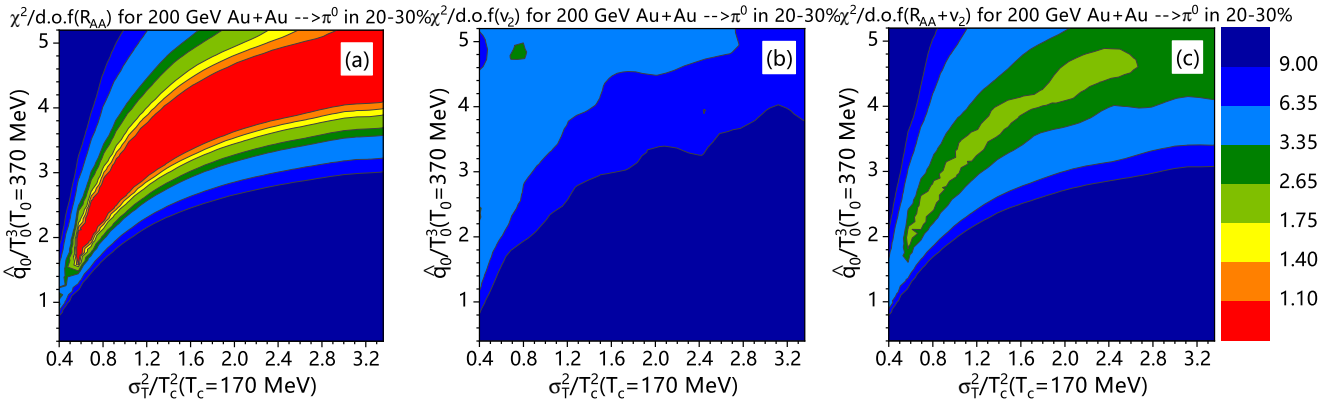

Fig. 10. (Gaussian-dependence) The $\chi^2/d.o.f$ analyses of single hadron $R_{AA}(p_{\rm T})$ (panel (a)) and elliptic flow $v_2(p_{\rm T})$ (panel (b)) as a function of σ_T^2/T_c^2 and $\hat{q}_0/T_0^3$ from fitting to experimental data [1–3] in 20 - 30% $Au+Au$ collisions at $\sqrt{s_{\rm NN}}=200$ GeV. The global $\chi^2/d.o.f$ fitting results for both $R_{AA}(p_{\rm T})$ and $v_2(p_{\rm T})$ are shown in the panel (c).

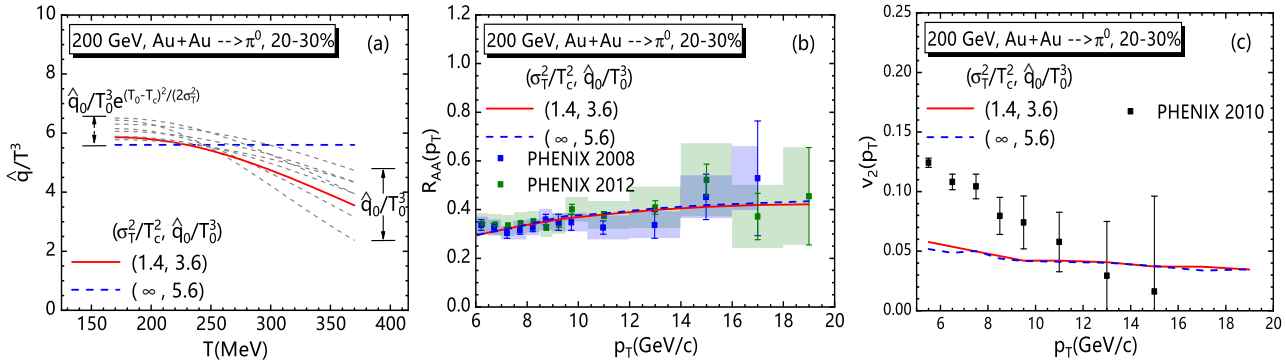

Fig. 11. (Gaussian-dependence) In 20 - 30% $Au+Au$ collisions at $\sqrt{s_{\rm NN}}=200$ GeV, the scaled dimensionless jet transport parameters $\hat{q}/T^3$ as a function of medium temperature T from the best fitting region of global χ^2 fits of Fig. 10 (c) are shown in panel (a). The single hadron suppression factors $R_{AA}(p_{\rm T})$ and elliptic flow parameter $v_2(p_{\rm T})$ are shown in panel (b) and (c), respectively, with couples of $(\sigma_T^2/T_c^2, \hat{q}_0/T_0^3)=(1.4, 3.6)$ (red solid curve) and $(\infty, 5.6)$ (blue dashed curve) compared with PHENIX [1–3] data.

ture dependence in 20 - 30% as well as in 0 - 5% centrality, $\chi^2/d.o.f(v_2)$ expresses a great favor in the small Gaussian width which gives $\hat{q}/T^3$ going down more rapidly with T. Consequently, the global $\chi^2/d.o.f$ fits for both $R_{AA}(p_{\rm T})$ and $v_2(p_{\rm T})$ give the explicit constraint for the introduced parameters $(\sigma_T^2/T_c^2, \hat{q}_0/T_0^3)$.

With the best global fitting values for $(\sigma_T^2/T_c^2, \hat{q}_0/T_0^3)$, we show in Fig. 11 (a) for the Gaussian T dependence of $\hat{q}/T^3$. Choosing the constant dependence with $(\sigma_T^2/T_c^2, \hat{q}_0/T_0^3)=(\infty, 5.6)$ (blue dashed curve) and a Gaussian T dependence with $(\sigma_T^2/T_c^2, \hat{q}_0/T_0^3)=(1.4, 3.6)$ (red solid curve) for $\hat{q}/T^3$, we again get the almost same $R_{AA}(p_{\rm T})$ as shown in Fig. 11 (b), and $v_2(p_{\rm T})$ with difference less than 5% in Fig. 11 (c). Compared to the case of the linearly-decreasing T dependence, the two $v_2(p_{\rm T})$ in Fig. 11 (c) are closer to each other because the difference between the Gaussian T dependence and the constant dependence is smaller, which leads to an almost invisible change in $v_2(p_{\rm T})$.

The use of a Gaussian form for $\hat{q}/T^3$ was intended to provide a more flexible temperature dependence by narrowing the Gaussian width compared to the linear form. Nevertheless, although v_2 data favor a higher Gaussian peak, while R_{AA} fitting imposes constraints on it. The global χ^2 fitting results for the Gaussian temperature dependence hypothesis presented in Fig. 11(a) did not manifest a steeper decline with increasing temperature. When comparing the red curve in Fig. 11(a) with that in Fig. 3(a), it is apparent that the linear temperature dependence results in a higher $\hat{q}_c/T_c^3$ at the critical temperature. And v_2 is more sensitive to energy loss near the critical temperature as stated previously. Therefore, the performance of the Gaussian shape is not much better than that of the linear shape.

B. Fit R_{AA} and v_2 at the LHC

Make the same process going through the case for $Pb+Pb$ collisions at $\sqrt{s_{\rm NN}}=2.76$ TeV. For the most central col-

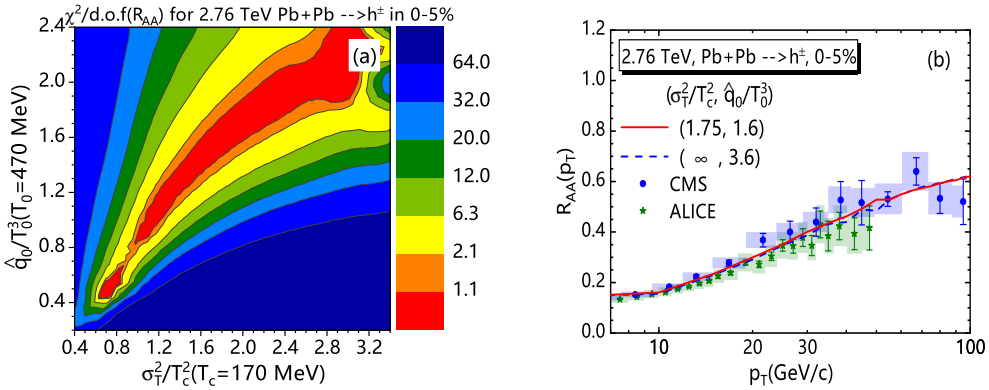

Fig. 12. (Gaussian-dependence) Panel (a): The $\chi^2/d.o.f$ analyses for single hadron $R_{AA}(p_{\rm T})$ as a function of $\hat{q}_c/T_c^3$ and $\hat{q}_0/T_0^3$ from fitting to experimental data [4, 5] in the most central 0 - 5% $Pb+Pb$ collisions at $\sqrt{s_{\rm NN}} = 2.76$ TeV. Panel (b): The single hadron suppression factors $R_{AA}(p_{\rm T})$ with couples of $(\sigma_T^2/T_c^2, \hat{q}_0/T_0^3) = (1.75, 1.6)$ (red solid curve) and $(\sigma_T^2/T_c^2, \hat{q}_0/T_0^3) = (\infty, 3.6)$ (blue dashed curve) compared with experimental data.

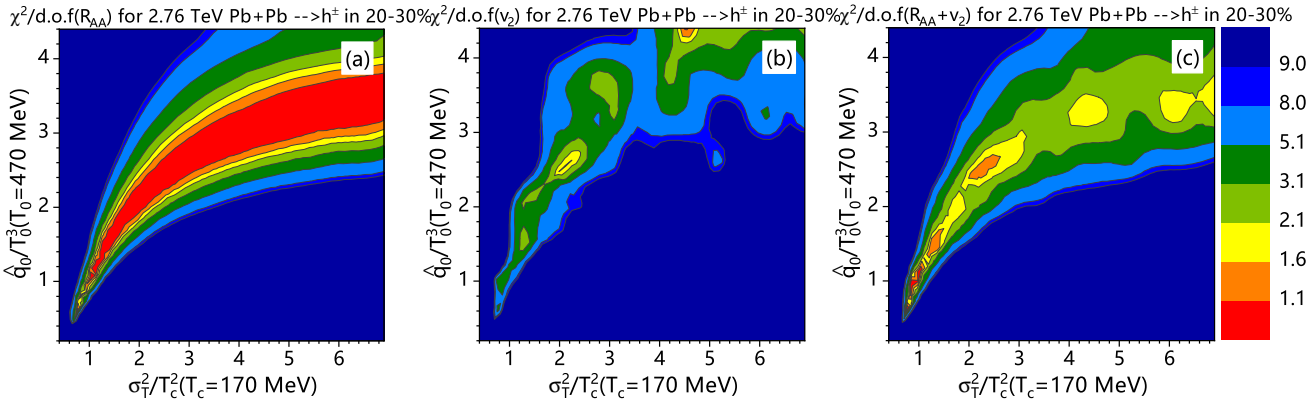

Fig. 13. (Gaussian-dependence) The $\chi^2/d.o.f$ analyses of single hadron $R_{AA}(p_{\rm T})$ (panel (a)) and elliptic flow $v_2(p_{\rm T})$ (panel (b)) as a function of σ_T^2/T_c^2 and $\hat{q}_0/T_0^3$ from fitting to experimental data [4, 5, 9, 10] in 20 - 30% $Pb+Pb$ collisions at $\sqrt{s_{\rm NN}} = 2.76$ TeV. The global $\chi^2/d.o.f$ fitting results for both $R_{AA}(p_{\rm T})$ and $v_2(p_{\rm T})$ are shown in panel (c).

lisions, we choose $\sigma_T^2/T_c^2 \in [0.35, 3.5]$ with bin size 0.35 and $\hat{q}_0/T_0^3 \in [0.2, 2.4]$ with bin size 0.2 and get 120 couples of $(\sigma_T^2/T_c^2, \hat{q}_0/T_0^3)$ to get $R_{AA}(p_{\rm T})$ and the 2-dimensional $\chi^2/d.o.f$ fitting contour plot, as shown in Fig. 12 (a). With the constant dependence with $(\sigma_T^2/T_c^2, \hat{q}_0/T_0^3) = (\infty, 3.6)$ and the Gaussian T dependence with $(\sigma_T^2/T_c^2, \hat{q}_0/T_0^3) = (1.75, 1.6)$, we get the same $R_{AA}(p_{\rm T})$ to fit data well, as shown in Fig. 12 (b).

For 20 - 30% collisions, we choose $\sigma_T^2/T_c^2 \in [0.35, 7.0]$ and $\hat{q}_0/T_0^3 \in [0.2, 4.4]$, and separately get 440 groups of $R_{AA}(p_{\rm T})$ and $v_2(p_{\rm T})$ to perform the $\chi^2/d.o.f$ fitting, as shown in Fig. 13 (a) and (b), respectively. The global fits for both $R_{AA}(p_{\rm T})$ and $v_2(p_{\rm T})$ are shown in Fig. 13 (c) where the constraints for the introduced parameters $(\sigma_T^2/T_c^2, \hat{q}_0/T_0^3)$ are obtained. With the constraints, the Gaussian T dependence of $\hat{q}/T^3$ is shown in Fig. 14 (a). Choosing a Gaussian T dependence with $(\sigma_T^2/T_c^2, \hat{q}_0/T_0^3) = (1.05, 1.2)$ (red solid curve) and the constant dependence with $(\sigma_T^2/T_c^2, \hat{q}_0/T_0^3) = (\infty, 4.1)$ (blue dashed curve) for $\hat{q}/T^3$, we again get almost the same $R_{AA}(p_{\rm T})$ shown in Fig. 14 (b), and different $v_2(p_{\rm T})$ in Fig. 14 (c). Compared to the constant case, the going-down Gaussian T dependence of $\hat{q}/T^3$ gives $v_2(p_{\rm T})$ an enhancement by about 10%.

Both at RHIC and the LHC, numerical results for simultaneously fitting to $R_{AA}(p_{\rm T})$ and $v_2(p_{\rm T})$ show that the Gaussian T dependence of $\hat{q}/T^3$ is smoothly going down with T and similar to the linearly-decreasing T dependence of $\hat{q}/T^3$. Compared with the constant $\hat{q}/T^3$, the going-down T dependence of $\hat{q}/T^3$ enhances the hadron azimuthal anisotropy by about 5-10% to improve $v_2(p_{\rm T})$ to fit data.

Thus far, we have demonstrated the constraining power of the experimental data on the three temperature-dependent forms of $\hat{q}/T^3$. To more clearly distinguish the separate constraining effects of R_{AA} and v_2, we have listed the best-fit parameters and the corresponding minimum $\chi^2/d.o.f$ values for each scenario in Table 1. These values correspond to the results shown in Figs. 2, 5,10, and 13. Note that for the constant form of $\hat{q}/T^3$, the v_2 data were not utilized.

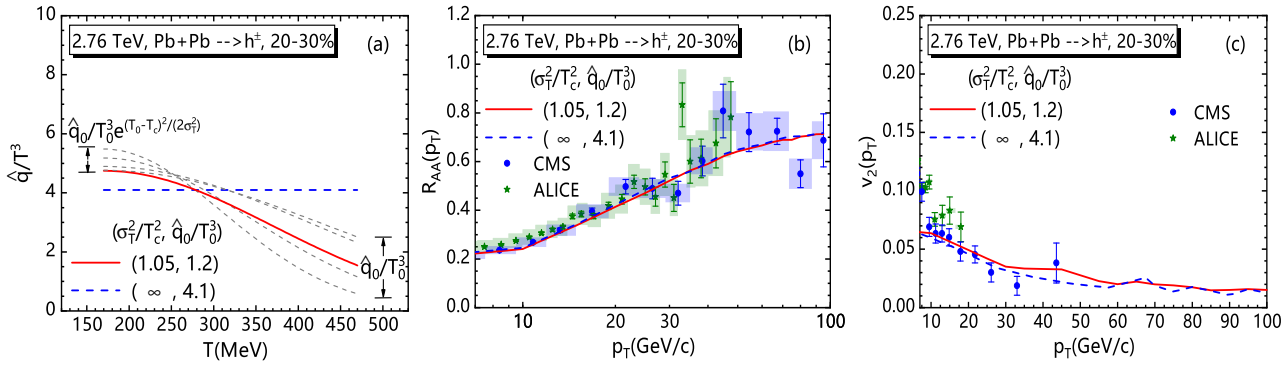

Fig. 14. (Gaussian-dependence) In 20 - 30% $Pb+Pb$ collisions at $\sqrt{s_{\rm NN}} = 2.76$ TeV, the scaled dimensionless jet transport parameters $\hat{q}/T^3$ as a function of medium temperature T from the best fitting region of global χ^2 fits of Fig. 13 (c) are shown in the panel (a). The single hadron suppression factors $R_{AA}(p_{\rm T})$ and elliptic flow $v_2(p_{\rm T})$ are shown in panels (b) and (c), respectively, with couples of $(\sigma_T^2/T_c^2, \hat{q}_0/T_0^3) = (1.05, 1.2)$ (red solid curve) and $(\infty, 4.1)$ (blue dashed curve) compared with experimental data [4, 5, 9, 10].

	Constant		Linear T dependence		Gaussian T dependence	
	$\hat{q}_c/T_c^3 = \hat{q}_0/T_0^3$	χ^2/d.o.f	$(\hat{q}_c/T_c^3, \hat{q}_0/T_0^3)$	χ^2/d.o.f	$(\sigma_T^2/T_c^2, \hat{q}_0/T_0^3)$	χ^2/d.o.f
20-30% $Au+Au$ collisions at 200 GeV						
R_{AA}	(5.8,5.8)	0.17	(6.9,1.1)	0.17	(2.8,4.4)	0.48
v_2	–	–	(8.7,0.5)	2.39	(0.4,2.4)	2.98
$(R_{AA}+v_2)$	–	–	(7.5,0.2)	1.51	(0.7,2.4)	2.45
20-30% $Pb+Pb$ collisions at 2.76 TeV						
R_{AA}	(4.0,4.0)	0.59	(5.0,3.6)	0.54	(4.8,3.2)	0.56
v_2	–	–	(5.4,0.2)	1.52	(2.1,2.4)	1.23
$(R_{AA}+v_2)$	–	–	(5.1,0.2)	0.94	(1.4,1.6)	1.23

TABLE 1. Optimal parameter and corresponding $\chi^2/d.o.f$ for different data sets in different $\hat{q}/T^3$ form. Note that for the constant form of $\hat{q}/T^3$, the v_2 data were not utilized.

V. LINEAR TEMPERATURE DEPENDENCE OF $\hat{q}/T^3$ IN QGP AND HADRON PHASES

In this section, for a total study of the linear temperature dependence of $\hat{q}/T^3$, we use Eqs. (10) (13) and (14) to include contributions from both QGP and hadron phases in 20 - 30% $A+A$ collisions.

A. Best fits for R_{AA} and v_2 due to energy loss in QGP and hadron phases

Let us begin with $Au+Au$ collisions in 20 - 30% at $\sqrt{s_{\rm NN}} = 200$ GeV. Shown in Fig. 15 are hadron suppression factors $R_{AA}(p_{\rm T})$ (panel (a)) and elliptic flow $v_2(p_{\rm T})$ (panel (b)) with jet energy loss of both QGP and hadronic phases (black solid curves) and of only QGP phase (red solid curves from Fig. 3) for 20 - 30% $Au+Au$ collisions at $\sqrt{s_{\rm NN}} = 200$ GeV, respectively. With the same $\hat{q}_0/T_0^3 = 0.2$ shown in Fig. 3, we have to decrease the value of $\hat{q}_c/T_c^3$ from 6.9 to 5.7 due to the included hadronic phase to get the same $R_{AA}(p_{\rm T})$. The reduction of 20% for $\hat{q}/T^3$ is consistent with a study in Ref. [23]. The jet energy loss in the hadron phase gives an enhancement by 10% for elliptic flow $v_2(p_{\rm T})$, which means the jet energy loss of the hadronic phase has an important and non-negligible contribution to $v_2(p_{\rm T})$.

As shown in Fig. 16 is for the case of 20 - 30% $Pb+Pb$ collisions at $\sqrt{s_{\rm NN}} = 2.76$ TeV. With the consistence $R_{AA}(p_{\rm T})$ in Fig. 16 (a), the $v_2(p_{\rm T})$ (black solid curve) with $(\hat{q}_c/T_c^3, \hat{q}_0/T_0^3) = (4.5, 0.0)$ of QGP phase and $\hat{q}_h$ of hadronic phase has an additional enhancement by 5% compared with $(\hat{q}_c/T_c^3, \hat{q}_0/T_0^3) = (5.4, 0.0)$ of only QGP phase (red solid curve from Fig. 6) in Fig. 16 (b). The enhancement is less than that at RHIC because the fraction of hadron phase contribution to jet energy loss at the LHC is less than that at RHIC, as shown in Fig. 17 (a) and (d).

It is worth noting that the description of $p_{\rm T}$ dependence of v_2 still deserves further improvement. This work only considers the T dependence of $\hat{q}/T^3$. Taking into account the dependence of $\hat{q}/T^3$ on parton energy E, which is more directly related to the $p_{\rm T}$ distribution of the jet energy loss [48, 50, 88], is likely to aid in improving the $p_{\rm T}$ dependence of v_2. Moreover, considering the dependence of $\hat{q}/T^3$ on the colliding energy $\sqrt{s_{\rm NN}}$ could also contribute to a more accurate description [89]. Additionally, elastic energy loss and jet-induced medium responses have a significant impact on

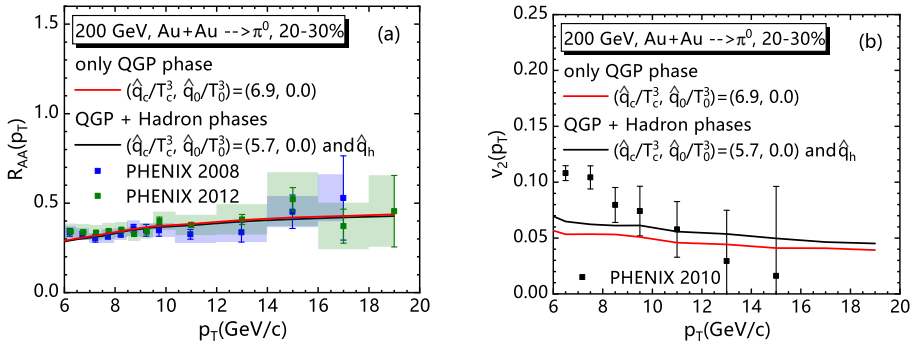

Fig. 15. Single hadron suppression factors $R_{AA}(p_{\rm T})$ (panel (a)) and elliptic flow $v_2(p_{\rm T})$ (panel (b)) with jet energy loss of QGP + Hadron phases (black solid curves with $(\hat{q}_c/T_c^3, \hat{q}_0/T_0^3) = (5.7, 0.0)$ and $\hat{q}_h$) and of only QGP phase (red solid curves with $(\hat{q}_c/T_c^3, \hat{q}_0/T_0^3) = (6.9, 0.0)$ from Fig. 3) for 20 - 30% $Au + Au$ collisions at $\sqrt{s_{\rm NN}} = 200$ GeV.

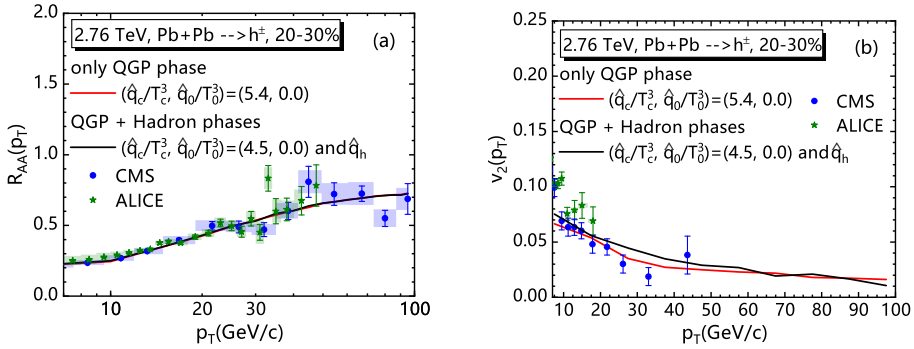

Fig. 16. Single hadron suppression factors $R_{AA}(p_{\rm T})$ (panel (a)) and elliptic flow $v_2(p_{\rm T})$ (panel (b)) with jet energy loss of both QGP + Hadron phases (black solid curves with $(\hat{q}_c/T_c^3, \hat{q}_0/T_0^3) = (4.5, 0.0)$ and $\hat{q}_h$) and of only QGP phase (red solid curves with $(\hat{q}_c/T_c^3, \hat{q}_0/T_0^3) = (5.4, 0.0)$ from Fig. 6) for 20 - 30% $Pb + Pb$ collisions at $\sqrt{s_{\rm NN}} = 2.76$ TeV.

hadron production at the intermediate transverse momentum, which could enhance the v_2 at this $p_{\rm T}$ region [90, 91]. We would incorporate these considerations into our model in the future to further improve its descriptive power for experimental data.

B. Jet energy loss distribution in QGP and hadron phases

Similarly to Fig. 7 and 8, we show in Fig. 17 the comparisons of the average jet energy loss distribution between QGP + Hadron phases (black solid curves) and only QGP phase (red solid curves) in noncentral $A + A$ collisions at RHIC (left panels) and the LHC (right panels), respectively. The black dot-dashed curves are for hadron phase contribution in the case of QGP + Hadron phases. From top to bottom are the average accumulative energy loss, differential energy loss, and the energy loss asymmetry, respectively.

The hadron phase contribution to the total energy loss of QGP + Hadron phases is about 17% at RHIC in Fig. 17 (a) while about 14% at the LHC in Fig. 17 (d). Because of the first order phase transition in the current model study shown in Fig. 7 (c) and (f), the hadron phase contribution happens mainly in the T_c nearby shown in Fig. 17 (b) and (e), which strengthens the azimuthal anisotropy of the system and then enhances the elliptic flow parameter. This is similar to the peak of the energy loss rate pushed to the T_c due to the going-down linear T dependence of $\hat{q}/T^3$ in Fig. 7 (b) and (e). Such enhancements of the azimuthal anisotropy are also exhibited by the energy loss asymmetry shown in Fig. 17 (c) and (f).

C. Temperature dependence of $\hat{q}/T^3$ in QGP and hadron phases

Shown in Fig. 18 is the $\hat{q}/T^3$ of the hadronic phase (dot-dashed line) and QGP phase (solid lines) as a function of medium temperature T. The hadronic phase $\hat{q}/T^3$ is given by Eq. (14). The values of $\hat{q}/T^3$ of QGP phase with the linear temperature dependence are given by Eq. (10) with $(\hat{q}_c/T_c^3, \hat{q}_0/T_0^3) = (5.7, 0.0)$ at RHIC (denoted in red curve) and $(4.5, 0.0)$ at the LHC (denoted in blue curve), respectively. The contributions to $\hat{q}/T^3$ of QGP and hadron phases combined via Eq. (13) are applied for $R_{AA}(p_{\rm T})$ and $v_2(p_{\rm T})$ at RHIC/LHC in Fig. 15 and Fig. 16. As comparisons, the

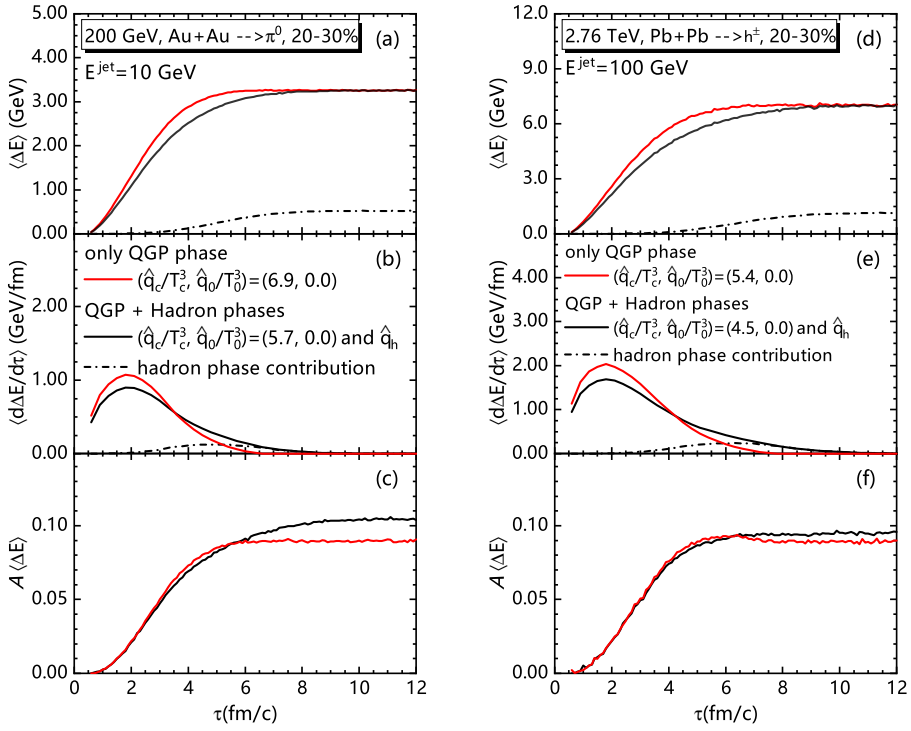

Fig. 17. Comparisons of the average jet energy loss distribution between QGP + Hadron phases (black solid curves) and only QGP phase (red solid curves from Fig. 7 and 8) in noncentral $A + A$ collisions at RHIC (left panels) and the LHC (right panels), respectively. The black dot-dashed curves are for hadron phase contribution in the case of QGP + Hadron phases. From top to bottom are the average accumulative energy loss, differential energy loss, and energy loss asymmetry, respectively.

representative samples of $\hat{q}/T^3$ extracted from single hadron, dihadron, and γ-hadron production at RHIC and the LHC energies with information field (IF) Bayesian analysis [51] are also shown in Fig. 18, which are denoted by grey curves. Ref. [51] do not consider the jet energy loss in the hadronic phase with a pseudocritical temperature $T_c = 0.165$ GeV. When considering the experimental data covering a wider temperature range, the $\hat{q}/T^3$ still points out a large value at the critical temperature. Our numerical results for the temperature-dependent $\hat{q}/T^3$ are consistent with that obtained by the IF-Bayesian method. After adding the hadron phase contribution to jet energy loss, one should decrease the QGP phase contribution so as to get the total energy loss equal to that for the case of only the QGP phase. The decreased QGP-phase energy loss makes $v_2(p_{\rm T})$ smaller while the added hadron-phase energy loss makes $v_2(p_{\rm T})$ larger. Numerical results show that the competition between them gives $v_2(p_{\rm T})$ larger than the case of only the QGP phase due to the energy loss contribution of the hadronic phase concentrating near the critical temperature. No matter the added hadron phase or the going-down linear T dependence of $\hat{q}/T^3$ in the QGP phase, as shown in Fig. 18, the jet is made to lose much more energy near the critical temperature, which results in a larger $v_2(p_{\rm T})$ for the large $p_{\rm T}$ to fit data better. Such a numerical result of the stronger jet quenching in the near-T_c region is consistent with a previous theoretical study [33]. One may notice that we extract the $\hat{q}/T^3$ at RHIC and the LHC with different parameter ranges. This is mainly because, in this work, we observed that extracting $\hat{q}/T^3$ at RHIC and the LHC separately could give a better χ^2 result compared to the simultaneous fit at both colliding energies. We only considered the dependence of $\hat{q}$ on temperature in this work. As mentioned previously, if the dependencies of $\hat{q}$ on parton energy E and $\sqrt{s_{\rm NN}}$, as well as the jet-induced medium responses and the elastic energy loss, were all taken into account, the value of $\hat{q}$ could be constrained more accurately from R_{AA} and v_2 at both RHIC and LHC energies simultaneously. Nevertheless, the $\hat{q}/T^3$ obtained in this work is also consistent with the $\hat{q}/T^3$ extracted by the IF-Bayesian approach [51] and the JETSCAPE [48, 50], which constrained the $\hat{q}/T^3$ from RHIC and the LHC simultaneously, as shown in Fig. 18. We hope that in the future, by updating the model and enriching the information on $\hat{q}$, we can better simultaneously describe the R_{AA} and v_2 for both RHIC and the LHC energies.

VI. SUMMARY

In this paper, within a next-to-leading-order perturbative QCD model, the medium temperature dependence of jet energy loss is studied via nuclear modification factor $R_{AA}(p_{\rm T})$ and elliptic flow parameter $v_2(p_{\rm T})$ of large transverse momentum hadrons. Due to jet quenching, medium-modified fragmentation functions based on the higher-twist energy loss

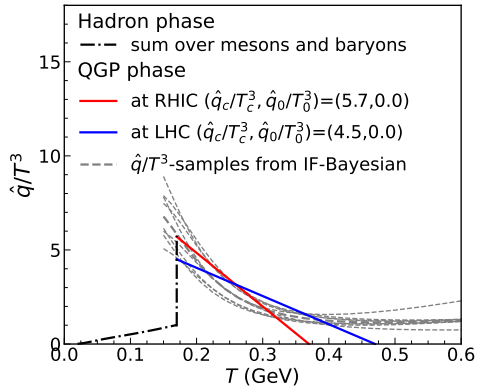

Fig. 18. The scaled jet transport coefficient $\hat{q}/T^3$ as a function of medium temperature T. $T < 0.17$ GeV for the hadronic phase (dot-dashed curve), and $T > 0.17$ GeV for the QGP phase (solid curves). The $\hat{q}/T^3$ of QGP phase for $Au + Au$ collisions at $\sqrt{s_{\rm NN}} = 200$ GeV is denoted in red and for $Pb + Pb$ collisions at $\sqrt{s_{\rm NN}} = 2.76$ TeV is denoted in blue. As comparisons, the $\hat{q}/T^3$ posterior samples from single hadron, dihadron, and γ-hadron production at RHIC and the LHC energies with IF-Bayesian analysis [51] are also shown in grey curves.

formalism are used in the numerical calculations. We assume the scaled jet transport coefficient $\hat{q}/T^3$ depends on medium temperature by linear or Gaussian form, with which we have calculated the single hadron suppression factor $R_{AA}(p_{\rm T})$ and the elliptic flow parameter $v_2(p_{\rm T})$ and compared them with experimental data. To constrain the $\hat{q}/T^3$ temperature dependence forms, a global χ^2 fitting has been performed on the the experimental data. Finally, the jet energy loss of the hadronic phase also has been taken into account.

With the linear T dependence of $\hat{q}/T^3$ for only the QGP phase, the global $\chi^2/d.o.f$ fitting for both $R_{AA}(p_{\rm T})$ and $v_2(p_{\rm T})$ shows that $\hat{q}_c/T_c^3 =$ 6.0-8.0 at RHIC and 4.0-6.0 at the LHC while $\hat{q}_0/T_0^3 =$ 0.0-4.2 at both RHIC and the LHC, as shown in Fig. 3 (a) and Fig. 6 (a). The numerical results show that $R_{AA}(p_{\rm T})$ and $v_2(p_{\rm T})$ are both more sensitive to the value of $\hat{q}/T^3$ near critical temperature T_c than near initial highest temperature T_0. Furthermore, the fitting results give a trend of the going-down $\hat{q}/T^3$ dependent on the medium temperature, which is also supported by the Gaussian T dependence of $\hat{q}/T^3$ for only the QGP phase.

Compared with the case of constant $\hat{q}/T^3$, the going-down T dependence of $\hat{q}/T^3$ makes a hard parton jet to lose more energy near the critical temperature T_c and therefore strengthens the azimuthal anisotropy for large $p_{\rm T}$ hadron productions. As a result, the elliptic flow parameter $v_2(p_{\rm T})$ for large $p_{\rm T}$ hadrons is enhanced by about 10% to fit data better at RHIC/LHC. Considering the first order phase transition from QGP to hadron and the hadron phase contribution to jet energy loss, $v_2(p_{\rm T})$ is again enhanced by 5-10% at RHIC/LHC.

ACKNOWLEDGMENTS

We would like to thank Xin-Nian Wang, Bowen Xiao and Guang-You Qin for excited discussions.

[1] A. Adare et al., Suppression pattern of neutral pions at high transverse momentum in Au+Au collisions at $\sqrt{s_{NN}} = 200$ GeV and constraints on medium transport coefficients. Phys. Rev. Lett. **101**, 232301 (2008). https://doi.org/10.1103/PhysRevLett.101.232301

[2] A. Adare et al., Neutral pion production with respect to centrality and reaction plane in Au+Au collisions at $\sqrt{s_{\rm NN}}$=200 GeV. Phys. Rev. C **87** no.3, 034911 (2013). https://doi.org/10.1103/PhysRevC.87.034911

[3] A. Adare et al., Azimuthal anisotropy of neutral pion production in Au+Au collisions at $\sqrt{s_{\rm NN}}$ = 200 GeV: Path-length dependence of jet quenching and the role of initial geometry. Phys. Rev. Lett. **105**, 142301 (2010). https://doi.org/10.1103/PhysRevLett.105.142301

[4] B. Abelev et al., Centrality Dependence of Charged Particle Production at Large Transverse Momentum in Pb–Pb Collisions at $\sqrt{s_{\rm NN}} = 2.76$ TeV. Phys. Lett. B **720**, 52-62 (2013). https://doi.org/10.1016/j.physletb.2013.01.051

[5] S. Chatrchyan et al., Study of High-pT Charged Particle Suppression in PbPb Compared to pp Collisions at $\sqrt{s_{\rm NN}} = 2.76$ TeV. Eur. Phys. J. C **72**, 1945 (2012). https://doi.org/10.1140/epjc/s10052-012-1945-x

[6] S. Acharya et al., Transverse momentum spectra and nuclear modification factors of charged particles in pp, p-Pb and Pb-Pb collisions at the LHC. JHEP **11**, 013 (2018). https://doi.org/10.1007/JHEP11(2018)013

[7] V. Khachatryan et al., Charged-particle nuclear modification factors in PbPb and pPb collisions at $\sqrt{s_{\rm NN}} = 5.02$ TeV. JHEP **04**, 039 (2017). https://doi.org/10.1007/JHEP04(2017)039

[8] S. Acharya et al., Transverse momentum spectra and nuclear modification factors of charged particles in Xe-Xe collisions at $\sqrt{s_{\rm NN}}$ = 5.44 TeV. Phys. Lett. B **788**, 166-179 (2019). https://doi.org/10.1016/j.physletb.2018.10.052

[9] S. Chatrchyan et al., Azimuthal Anisotropy of Charged Particles at High Transverse Momenta in PbPb Collisions at $\sqrt{s_{\rm NN}} = 2.76$ TeV. Phys. Rev. Lett. **109**, 022301 (2012). https://doi.org/10.1103/PhysRevLett.109.022301

[10] B. Abelev et al., Anisotropic flow of charged hadrons, pions and (anti-)protons measured at high transverse momentum in Pb-Pb collisions at $\sqrt{s_{\rm NN}}$=2.76 TeV. Phys. Lett. B **719**, 18-28 (2013). https://doi.org/10.1016/j.physletb.2012.12.066

[11] J. Adam et al., Anisotropic flow of charged particles in Pb-Pb collisions at $\sqrt{s_{\rm NN}} = 5.02$ TeV. Phys. Rev. Lett. **116**, 132302 (2016). https://doi.org/10.1103/PhysRevLett.116.132302

[12] A. M. Sirunyan et al., Azimuthal anisotropy of charged particles with transverse momentum up to 100 GeV/c in PbPb collisions at $\sqrt{s_{\rm NN}}$=5.02 TeV. Phys. Lett. B **776**, 195-216 (2018). https://doi.org/10.1016/j.physletb.2017.11.041

[13] M. Gyulassy and M. Plumer, Jet Quenching in Dense Matter. Phys. Lett. B **243**, 432-438 (1990). https://doi.org/10.1016/0370-2693(90)91409-5

[14] X. N. Wang and M. Gyulassy, Gluon shadowing and jet quenching in A + A collisions at $\sqrt{s_{\rm NN}}$ =

200 GeV. Phys. Rev. Lett. **68**, 1480-1483 (1992). https://doi.org/10.1103/PhysRevLett.68.1480
[15] G. Y. Qin and X. N. Wang, Jet quenching in high-energy heavy-ion collisions. Int. J. Mod. Phys. E **24**, 1530014 (2015). https://doi.org/10.1142/S0218301315300143
[16] Z. W. Lin and L. Zheng, Further developments of a multi-phase transport model for relativistic nuclear collisions. Nucl. Sci. Tech. **32**, 113 (2021). https://doi.org/10.1007/s41365-021-00944-5
[17] Z. Tang, Z. B. Tang, W. Zha, W. M. Zha, Y. Zhang and Y. F. Zhang, An experimental review of open heavy flavor and quarkonium production at RHIC. Nucl. Sci. Tech. **31**, 81 (2020). https://doi.org/10.1007/s41365-020-00785-8
[18] L. Ma, X. Dong, H. Z. Huang and Y. G. Ma, Study of a background reconstruction method for the measurement of D-meson azimuthal angular correlations. Nucl. Sci. Tech. **32**, 61 (2021). https://doi.org/10.1007/s41365-021-00896-w
[19] H. Song, Y. Zhou and K. Gajdosova, Collective flow and hydrodynamics in large and small systems at the LHC. Nucl. Sci. Tech. **28**, 99 (2017). https://doi.org/10.1007/s41365-017-0245-4
[20] X. Luo and N. Xu, Search for the QCD Critical Point with Fluctuations of Conserved Quantities in Relativistic Heavy-Ion Collisions at RHIC : An Overview. Nucl. Sci. Tech. **28**, 112 (2017). https://doi.org/10.1007/s41365-017-0257-0
[21] R. Baier, Y. L. Dokshitzer, A. H. Mueller, S. Peigne and D. Schiff, Radiative energy loss and p(T) broadening of high-energy partons in nuclei. Nucl. Phys. B **484**, 265-282 (1997). https://doi.org/10.1016/S0550-3213(96)00581-0
[22] K. M. Burke et al., Extracting the jet transport coefficient from jet quenching in high-energy heavy-ion collisions. Phys. Rev. C **90**, 014909 (2014). https://doi.org/10.1103/PhysRevC.90.014909
[23] X. F. Chen, C. Greiner, E. Wang, X. N. Wang and Z. Xu, Bulk matter evolution and extraction of jet transport parameter in heavy-ion collisions at RHIC. Phys. Rev. C **81**, 064908 (2010). https://doi.org/10.1103/PhysRevC.81.064908
[24] X. F. Chen, T. Hirano, E. Wang, X. N. Wang and H. Zhang, Suppression of high p_T hadrons in $Pb + Pb$ Collisions at LHC. Phys. Rev. C **84**, 034902 (2011). https://doi.org/10.1103/PhysRevC.84.034902
[25] M. Xie, S. Y. Wei, G. Y. Qin and H. Z. Zhang, Extracting jet transport coefficient via single hadron and dihadron productions in high-energy heavy-ion collisions. Eur. Phys. J. C **79**, 589 (2019). https://doi.org/10.1140/epjc/s10052-019-7100-1
[26] Z. Q. Liu, H. Zhang, B. W. Zhang and E. Wang, Quantifying jet transport properties via large p_T hadron production. Eur. Phys. J. C **76**, 20 (2016). https://doi.org/10.1140/epjc/s10052-016-3885-3
[27] B. Schenke, C. Gale and S. Jeon, MARTINI: An Event generator for relativistic heavy-ion collisions. Phys. Rev. C **80**, 054913 (2009). https://doi.org/10.1103/PhysRevC.80.054913
[28] G. Y. Qin, J. Ruppert, C. Gale, S. Jeon, G. D. Moore and M. G. Mustafa, Radiative and collisional jet energy loss in the quark-gluon plasma at RHIC. Phys. Rev. Lett. **100**, 072301 (2008). https://doi.org/10.1103/PhysRevLett.100.072301
[29] S. K. Das, F. Scardina, S. Plumari and V. Greco, Toward a solution to the R_{AA} and v_2 puzzle for heavy quarks. Phys. Lett. B **747**, 260-264 (2015). https://doi.org/10.1016/j.physletb.2015.06.003
[30] S. Cao, L. G. Pang, T. Luo, Y. He, G. Y. Qin and X. N. Wang, R_{AA} vs. v_2 of heavy and light hadrons within a linear Boltzmann transport model. Nucl. Part. Phys. Proc. **289-290**, 217-220 (2017). https://doi.org/10.1016/j.nuclphysbps.2017.05.048
[31] X. N. Wang, Dynamical screening and radiative parton energy loss in a quark gluon plasma. Phys. Lett. B **485**, 157-161 (2000). https://doi.org/10.1016/S0370-2693(00)00642-0
[32] J. Casalderrey-Solana and X. N. Wang, Energy dependence of jet transport parameter and parton saturation in quark-gluon plasma. Phys. Rev. C **77**, 024902 (2008). https://doi.org/10.1103/PhysRevC.77.024902
[33] J. Liao and E. Shuryak, Angular Dependence of Jet Quenching Indicates Its Strong Enhancement Near the QCD Phase Transition. Phys. Rev. Lett. **102**, 202302 (2009). https://doi.org/10.1103/PhysRevLett.102.202302
[34] J. Xu, J. Liao and M. Gyulassy, Consistency of Perfect Fluidity and Jet Quenching in semi-Quark-Gluon Monopole Plasmas. Chin. Phys. Lett. **32**, 092501 (2015). https://doi.org/10.1088/0256-307X/32/9/092501
[35] J. Xu, J. Liao and M. Gyulassy, Bridging Soft-Hard Transport Properties of Quark-Gluon Plasmas with CUJET3.0. JHEP **02**, 169 (2016). https://doi.org/10.1007/JHEP02(2016)169
[36] S. Shi, J. Liao and M. Gyulassy, Global constraints from RHIC and LHC on transport properties of QCD fluids in CUJET/CIBJET framework. Chin. Phys. C **43**, 044101 (2019). https://doi.org/10.1088/1674-1137/43/4/044101
[37] M. Gyulassy, P. Levai and I. Vitev, Reaction operator approach to nonAbelian energy loss. Nucl. Phys. B **594**, 371-419 (2001). https://doi.org/10.1016/S0550-3213(00)00652-0
[38] B. Wu, Radiative energy loss and radiative $p_\perp$-broadening of high-energy partons in QCD matter. JHEP **12**, 081 (2014). https://doi.org/10.1007/JHEP12(2014)081
[39] A. H. Mueller, B. Wu, B. W. Xiao and F. Yuan, Medium Induced Transverse Momentum Broadening in Hard Processes. Phys. Rev. D **95**, 034007 (2017). https://doi.org/10.1103/PhysRevD.95.034007
[40] E. Iancu, P. Taels and B. Wu, Jet quenching parameter in an expanding QCD plasma. Phys. Lett. B **786**, 288-295 (2018). https://doi.org/10.1016/j.physletb.2018.10.007
[41] H. Liu, K. Rajagopal and U. A. Wiedemann, Calculating the jet quenching parameter from AdS/CFT. Phys. Rev. Lett. **97**, 182301 (2006). https://doi.org/10.1103/PhysRevLett.97.182301
[42] Z. q. Zhang, D. f. Hou, Y. Wu and G. Chen, R^2 Corrections to the Jet Quenching Parameter. Adv. High Energy Phys. **2016**, 9503491 (2016). https://doi.org/10.1155/2016/9503491
[43] J. Ghiglieri and H. Kim, Transverse momentum broadening and collinear radiation at NLO in the $\mathcal{N} = 4$ SYM plasma. JHEP **12**, 049 (2018). https://doi.org/10.1007/JHEP12(2018)049
[44] M. Panero, K. Rummukainen and A. Schäfer, Lattice Study of the Jet Quenching Parameter. Phys. Rev. Lett. **112**, 162001 (2014). https://doi.org/10.1103/PhysRevLett.112.162001
[45] M. Panero, K. Rummukainen and A. Schäfer, Investigating jet quenching on the lattice. Nucl. Phys. A **932**, 122-127 (2014). https://doi.org/10.1016/j.nuclphysa.2014.07.008
[46] M. Panero, K. Rummukainen and A. Schäfer, Jet quenching from the lattice. Nucl. Phys. A **931**, 393-398 (2014). https://doi.org/10.1016/j.nuclphysa.2014.07.037
[47] A. Kumar, A. Majumder and C. Nonaka, First calculation of $\hat{q}$ on a quenched SU(3) plasma. PoS **LATTICE2018**, 169 (2018). https://doi.org/10.22323/1.334.0169
[48] S. Cao et al., Determining the jet transport coefficient $\hat{q}$ from inclusive hadron suppression measurements using Bayesian parameter estimation. Phys. Rev. C **104**, 024905 (2021). https://doi.org/10.1103/PhysRevC.104.024905

[49] W. Ke and X. N. Wang, QGP modification to single inclusive jets in a calibrated transport model. JHEP **05**, 041 (2021). https://doi.org/10.1007/JHEP05(2021)041

[50] A. Kumar et al., Inclusive jet and hadron suppression in a multistage approach. Phys. Rev. C **107**, 034911 (2023). https://doi.org/10.1103/PhysRevC.107.034911

[51] M. Xie, W. Ke, H. Zhang and X. N. Wang, Information-field-based global Bayesian inference of the jet transport coefficient. Phys. Rev. C **108**, L011901 (2023). https://doi.org/10.1103/PhysRevC.108.L011901

[52] W. t. Deng and X. N. Wang, Multiple Parton Scattering in Nuclei: Modified DGLAP Evolution for Fragmentation Functions. Phys. Rev. C **81**, 024902 (2010). https://doi.org/10.1103/PhysRevC.81.024902

[53] E. Wang and X. N. Wang, Parton energy loss with detailed balance. Phys. Rev. Lett. **87**, 142301 (2001). https://doi.org/10.1103/PhysRevLett.87.142301

[54] E. Wang and X. N. Wang, Jet tomography of dense and nuclear matter. Phys. Rev. Lett. **89**, 162301 (2002). https://doi.org/10.1103/PhysRevLett.89.162301

[55] T. Hirano, Is early thermalization achieved only near mid-rapidity at RHIC? Phys. Rev. C **65**, 011901 (2002). https://doi.org/10.1103/PhysRevC.65.011901

[56] T. Hirano and K. Tsuda, Collective flow and two pion correlations from a relativistic hydrodynamic model with early chemical freezeout. Phys. Rev. C **66**, 054905 (2002). https://doi.org/10.1103/PhysRevC.66.054905

[57] J. F. Owens, Large Momentum Transfer Production of Direct Photons, Jets, and Particles. Rev. Mod. Phys. **59**, 465 (1987). https://doi.org/10.1103/RevModPhys.59.465

[58] R. Brock et al., Handbook of perturbative QCD: Version 1.0. Rev. Mod. Phys. **67**, 157-248 (1995). https://doi.org/10.1103/RevModPhys.67.157

[59] T. J. Hou, S. Dulat, J. Gao, M. Guzzi, J. Huston, P. Nadolsky, J. Pumplin, C. Schmidt, D. Stump and C. P. Yuan, CTEQ-TEA parton distribution functions and HERA Run I and II combined data. Phys. Rev. D **95**, 034003 (2017). https://doi.org/10.1103/PhysRevD.95.034003

[60] S. Albino, B. A. Kniehl and G. Kramer, AKK Update: Improvements from New Theoretical Input and Experimental Data. Nucl. Phys. B **803**, 42-104 (2008). https://doi.org/10.1016/j.nuclphysb.2008.05.017

[61] B. W. Harris and J. F. Owens, The Two cutoff phase space slicing method. Phys. Rev. D **65**, 094032 (2002). https://doi.org/10.1103/PhysRevD.65.094032

[62] H. Zhang, J. F. Owens, E. Wang and X. N. Wang, Dihadron tomography of high-energy nuclear collisions in NLO pQCD. Phys. Rev. Lett. **98**, 212301 (2007). https://doi.org/10.1103/PhysRevLett.98.212301

[63] H. Zhang, J. F. Owens, E. Wang and X. N. Wang, Tomography of high-energy nuclear collisions with photon-hadron correlations. Phys. Rev. Lett. **103**, 032302 (2009). https://doi.org/10.1103/PhysRevLett.103.032302

[64] X. N. Wang, pQCD based approach to parton production and equilibration in high-energy nuclear collisions. Phys. Rept. **280**, 287-371 (1997). https://doi.org/10.1016/S0370-1573(96)00022-1

[65] S. y. Li and X. N. Wang, Gluon shadowing and hadron production at RHIC. Phys. Lett. B **527**, 85-91 (2002). https://doi.org/10.1016/S0370-2693(02)01179-6

[66] V. Emel'yanov, A. Khodinov, S. R. Klein and R. Vogt, The Effect of shadowing on initial conditions, transverse energy and hard probes in ultrarelativistic heavy ion collisions. Phys. Rev. C **61**, 044904 (2000). https://doi.org/10.1103/PhysRevC.61.044904

[67] T. Hirano and Y. Nara, Interplay between soft and hard hadronic components for identified hadrons in relativistic heavy ion collisions at RHIC. Phys. Rev. C **69**, 034908 (2004). https://doi.org/10.1103/PhysRevC.69.034908

[68] K. J. Eskola, P. Paakkinen, H. Paukkunen and C. A. Salgado, EPPS16: Nuclear parton distributions with LHC data. Eur. Phys. J. C **77**, 163 (2017). https://doi.org/10.1140/epjc/s10052-017-4725-9

[69] X. N. Wang, Z. Huang and I. Sarcevic, Jet quenching in the opposite direction of a tagged photon in high-energy heavy ion collisions. Phys. Rev. Lett. **77**, 231-234 (1996). https://doi.org/10.1103/PhysRevLett.77.231

[70] X. N. Wang and Z. Huang, Study medium induced parton energy loss in gamma + jet events of high-energy heavy ion collisions. Phys. Rev. C **55**, 3047-3061 (1997). https://doi.org/10.1103/PhysRevC.55.3047

[71] X. N. Wang, Energy dependence of jet quenching and life-time of the dense matter in high-energy heavy-ion collisions. Phys. Rev. C **70**, 031901 (2004). https://doi.org/10.1103/PhysRevC.70.031901

[72] N. B. Chang, W. T. Deng and X. N. Wang, Initial conditions for the modified evolution of fragmentation functions in the nuclear medium. Phys. Rev. C **89**, 034911 (2014). https://doi.org/10.1103/PhysRevC.89.034911

[73] B. W. Zhang and X. N. Wang, Multiple parton scattering in nuclei: Beyond helicity amplitude approximation. Nucl. Phys. A **720**, 429-451 (2003). https://doi.org/10.1016/S0375-9474(03)01003-0

[74] B. W. Zhang, E. k. Wang and X. N. Wang, Multiple parton scattering in nuclei: Heavy quark energy loss and modified fragmentation functions. Nucl. Phys. A **757**, 493-524 (2005). https://doi.org/10.1016/j.nuclphysa.2005.04.022

[75] N. Armesto, B. Cole, C. Gale, W. A. Horowitz, P. Jacobs, S. Jeon, M. van Leeuwen, A. Majumder, B. Muller and G. Y. Qin, et al., Comparison of Jet Quenching Formalisms for a Quark-Gluon Plasma 'Brick'. Phys. Rev. C **86**, 064904 (2012). https://doi.org/10.1103/PhysRevC.86.064904

[76] S. Cao, G. Coci, S. K. Das, W. Ke, S. Y. F. Liu, S. Plumari, T. Song, Y. Xu, J. Aichelin and S. Bass, et al., Toward the determination of heavy-quark transport coefficients in quark-gluon plasma. Phys. Rev. C **99**, 054907 (2019). https://doi.org/10.1103/PhysRevC.99.054907

[77] S. Shi, J. Liao and M. Gyulassy, Global constraints from RHIC and LHC on transport properties of QCD fluids in CUJET/CIBJET framework. Chin. Phys. C **43**, 044101 (2019). https://doi.org/10.1088/1674-1137/43/4/044101

[78] W. Dai, S. Wang, S. L. Zhang, B. W. Zhang and E. Wang, Transverse Momentum Balance and Angular Distribution of $b\bar{b}$ Dijets in Pb+Pb collisions. Chin. Phys. C **44**, 104105 (2020). https://doi.org/10.1088/1674-1137/abab8f

[79] C. Nonaka, E. Honda and S. Muroya, (3+1)-dimensional relativistic hydrodynamical expansion of hot and dense matter in ultrarelativistic nuclear collision. Eur. Phys. J. C **17**, 663-673 (2000). https://doi.org/10.1007/s100520000509

[80] T. Hirano, U. W. Heinz, D. Kharzeev, R. Lacey and Y. Nara, Mass ordering of differential elliptic flow and its violation for phi mesons. Phys. Rev. C **77**, 044909 (2008). https://doi.org/10.1103/PhysRevC.77.044909

[81] H. Wang and J. H. Chen, Study on open charm hadron production and angular correlation in high-energy nuclear collisions. Nucl. Sci. Tech. **32**, 2 (2021). https://doi.org/10.1007/s41365-

020-00839-x

[82] A. M. Poskanzer and S. A. Voloshin, Methods for analyzing anisotropic flow in relativistic nuclear collisions. Phys. Rev. C **58**, 1671-1678 (1998). https://doi.org/10.1103/PhysRevC.58.1671

[83] X. N. Wang, Jet quenching and azimuthal anisotropy of large p(T) spectra in noncentral high-energy heavy ion collisions. Phys. Rev. C **63**, 054902 (2001). https://doi.org/10.1103/PhysRevC.63.054902

[84] S. Y. Tang, L. Zheng, X. M. Zhang and R. Z. Wan, Investigating the elliptic anisotropy of identified particles in p–Pb collisions with a multi-phase transport model. Nucl. Sci. Tech. **35**, 32 (2024). https://doi.org/10.1007/s41365-024-01387-4

[85] M. Wang, J. Q. Tao, H. Zheng, W. C. Zhang, L. L. Zhu and A. Bonasera, Number-of-constituent-quark scaling of elliptic flow: a quantitative study. Nucl. Sci. Tech. **33**, 37 (2022). https://doi.org/10.1007/s41365-022-01019-9

[86] S. W. Lan and S. S. Shi, Anisotropic flow in high baryon density region. Nucl. Sci. Tech. **33**, 21 (2022). https://doi.org/10.1007/s41365-022-01006-0

[87] H. Wang and J. H. Chen, Anisotropy flows in Pb–Pb collisions at LHC energies from parton scatterings with heavy quark trigger. Nucl. Sci. Tech. **33**, 15 (2022). https://doi.org/10.1007/s41365-022-00999-y

[88] Y. He, L. G. Pang and X. N. Wang, Bayesian extraction of jet energy loss distributions in heavy-ion collisions. Phys. Rev. Lett. **122**, 252302 (2019). https://doi.org/10.1103/PhysRevLett.122.252302

[89] L. L. Zhu, B. Wang, M. Wang and H. Zheng, Energy and centrality dependence of light nuclei production in relativistic heavy-ion collisions. Nucl. Sci. Tech. **33**, 45 (2022). https://doi.org/10.1007/s41365-022-01028-8

[90] G. Y. Qin, Anisotropic Flow and Jet Quenching in Relativistic Nuclear Collisions. Int. J. Mod. Phys. E **24**, 1530001 (2015). https://doi.org/10.1142/S0218301315300015

[91] W. Zhao, W. Ke, W. Chen, T. Luo and X. N. Wang, From Hydrodynamics to Jet Quenching, Coalescence, and Hadron Cascade: A Coupled Approach to Solving the RAA⊗v2 Puzzle. Phys. Rev. Lett. **128**, 022302 (2022). https://doi.org/10.1103/PhysRevLett.128.022302